Electrical transport modelling in organic electroluminescent devices

2002 J. Phys.: Condens. Matter 14 9825

(http://iopscience.iop.org/0953-8984/14/42/303)

INSTITUTE OF PHYSICS PUBLISHING JOURNAL OF PHYSICS: CONDENSED MATTER

J. Phys.: Condens. Matter **14** (2002) 9825–9876 PII: S0953-8984(02)33486-6

Electrical transport modelling in organic electroluminescent devices

A B Walker[1], **A Kambili and S J Martin**

Department of Physics, University of Bath, Bath BA2 7AY, UK

E-mail: a.b.walker@bath.ac.uk

Received 5 February 2002, in final form 23 May 2002
Published 11 October 2002
Online at stacks.iop.org/JPhysCM/14/9825

Abstract

Organic electroluminescent devices (OEDs) emit light when an electric current is applied to a thin film section. They arise from two main technology branches—small molecules and light emitting polymers. Apart from the insight offered into the fundamentals of their physics, which is relevant to topics such as electrical transport in biological systems and molecular computers, understanding how the mobilities in these systems vary with morphology and composition enables the design of improved materials for technological requirements, e.g. fast switching speeds for active matrix displays and polymer field effect transistors. In this review, we have focussed on the models of transport in OEDs that address the unusual nature of this transport and underpin device design. The review concludes with the following point: as new materials for use in OEDs continue to appear, modelling is essential for the prediction of their transport properties, which in turn leads to the establishment of fundamental trends in the behaviour of devices employing them.

Contents

[1] Author to whom any correspondence should be addressed.

1. Introduction

Organic electroluminescence is the emission of light from thin films of organic materials as a result of electrical excitation. It occurs in organic electroluminescent devices (OEDs) when electrons are injected from an electrode on one side of the film and holes from the other, and an exciton (a bound state) is formed from the capture of oppositely charged carriers that can decay radiatively. OEDs arise from two main technology branches—on the one hand, we have small-molecule devices, and, on the other, those based on small molecules and light-emitting polymers. Commercial interest in active and passive matrix displays based on OEDs as a new display technology comes from their exploitation in thin, lightweight displays which can be flexible or flat panel with full colour and high image content, and are characterized by low manufacturing costs. Key advantages of OEDs are:

(a) organic materials form thin solid films with luminous emissive layers;
(b) the emission wavelengths can be tuned by blending, in the case of light-emitting polymers, or by the incorporation of suitable fluorescent dyes in the emissive layers for small-molecule devices;
(c) the forward drive voltages are <10 V;
(d) high emission efficiencies can been reached, e.g. internal quantum efficiencies of 10% have been measured;
(e) the devices have wide viewing angles;
(f) they exhibit fast response.

Small-molecule-based displays are being developed by Kodak and can already be found in car automotive components manufactured by Pioneer, and cellular phones marketed by Motorola and Sanyo. Philips and Cambridge Display Technology amongst others are developing light-emitting polymer technology for mobile communications. These materials also have many electronic applications, such as in polymer field effect transistors for use in product tagging and bar codes that can be read remotely [1].

Despite the rapid progress towards commercial applications, device modelling is required to understand the physics underpinning transport in these materials. Apart from the insight offered into the fundamentals of physics, which bears on related topics such as electrical transport in biological systems and molecular computers, understanding how the mobilities in these systems vary with morphology and composition enables the design of improved materials for technological requirements, such as fast switching speeds for active matrix displays and polymer field effect transistors [2]. Mobilities of the order of 0.01 $cm^2\ V^{-1}\ s^{-1}$ and above have been achieved through different techniques, e.g. in polyfluorene films on rubbed polyimide [3].

Whilst electroluminescence in organic materials has been known for over 40 years [4], the first demonstration that OEDs would be viable for displays is widely acknowledged to be the work of Tang and VanSlyke [5]. They showed that in a device with a layer of an aromatic diamine and a layer of 8-hydroxyquinoline aluminium (Alq_3), the latter being the

luminescent layer, high external quantum efficiency, luminous efficiency, and brightness were achievable at driving voltages below 10 V. Molecular orbital calculations of the electronic structure of Alq_3 [6] have given the energies of the filled orbitals, particularly the highest occupied molecular orbital (HOMO) state and lowest unoccupied molecular orbital (LUMO) state. The HOMO and LUMO states are equivalent to the top of the valence band and the bottom of the conduction band of inorganic materials, respectively. Conduction is thought to proceed by hopping between LUMO states and may be limited by a high density of traps. Burrows *et al* [6] have shown that the trap distribution deduced from measured current–voltage data is consistent with small conformational distortions of the Alq_3 molecule.

Burroughes *et al* [7] showed in 1990 that OEDs fabricated from a single layer of conjugated polymers, such as polyphenylene vinylene (PPV), are also characterized by good charge transport and high quantum efficiency. In such polymers, three of the four electrons in the outer shell of carbon occupy sp^2 hybridized states, creating the bonds that form the polymer backbone. Since the σ bonds provide a strong structural framework, there are no dangling bonds and, therefore, the interfaces are not so sensitive to the environment. The remaining electron, occupying a p_z orbital, overlaps with similar electrons from neighbouring carbon atoms to form a delocalized π electron system along the polymer backbone. To lower the energy, the π orbitals form alternate single and double bonds giving rise to the conjugation of the polymer backbone, opening an energy gap between the filled bonding states (the HOMO or valence band) and the empty antibonding states (the LUMO or conduction band). This band structure confers semiconducting properties to the polymer and gives it the ability to support positive and negative charge carriers.

Each polymer chain consists of a number of conjugated segments separated by twists or kinks that disrupt the π bonds and cause each segment to behave like a separate entity. The distribution of segment lengths results in a distribution of electron states, and the polymers show only partial crystallinity; the chains are not aligned with each other over their whole length, but only in small crystal regions of typical dimensions 10–50 nm. The polymer chains may either extend through a number of crystallite regions or may be folded back on themselves within these regions. In either case, ordered crystallites are interconnected by amorphous regions [8]. Such a morphology modifies the electron states in each segment because the electron polarizability of the surrounding medium varies and because of local dipole interactions between neighbouring chains. This effect, combined with the distribution of segment lengths, broadens the electronic density of states by about 0.1–0.2 eV [9] and results in hopping-type transport. Charging of a polymer chain during transport results in its accompanying distortion around charged excitations, which are described as polarons in these materials. In the literature, however, polarons are usually referred to as electrons or holes.

The charged excitations recombine, forming excitons. An exciton in organic materials is generally more localized than in inorganic semiconductors as it is confined to a molecule for the small-molecules case or to a segment for the polymers case. Consequently, the exchange energy, and hence the singlet–triplet separation, is large, so crossover from triplet to singlet states is unlikely. Spin-allowed radiative emission (fluorescence) is only possible between singlet states, so light emission from triplets can only occur indirectly through processes such as triplet–triplet annihilation or phosphorescence. If the process by which these states form is spin independent, the maximum efficiency of organic LEDs is limited to 25%, but the efficiency can be improved if this restriction is broken through spin–orbit coupling to atoms, e.g. platinum, introduced into the polymer [10].

Carrier transport in amorphous solids has attracted much attention since the 1950s when it came to the fore as a result of the need to understand xerographic materials [11]. Electronic processes in amorphous materials involve concepts such as the mobility edge, which

separates localized from extended states [12]. In localized states, the mobility vanishes at zero temperature even though the wavefunctions of neighbouring states overlap. At non-zero temperatures, hopping transport between localized sites is the rate-determining step. This point has been confirmed by experimental observations that μ takes the Poole–Frenkel form characteristic of hopping transport in disordered materials, described in section 3.

In general, device modelling provides a useful tool, facilitating device design. Analysis of experimental data in the earliest papers on OEDs focused on the space-charge-limited current (SCLC) on the basis that the mobilities in these materials were approximately $10^{-5}\,\mathrm{cm}^2\,\mathrm{V}^{-1}\,\mathrm{s}^{-1}$ and thus about nine orders of magnitude lower than typical mobilities in crystalline inorganic semiconductors. Space charge builds up in the material, leading to Child's law in which the current density is $J \propto V^2$, where V is the applied bias. Analytical models have also been developed for trap-limited SCLC, including those that are valid for the Poole–Frenkel mobility [13, 14]. Such models give a power law behaviour of the J–V data that has been shown to give very good agreement with experiments, even though it has been argued that the injection processes at the metal–organic contact dominate the J–V characteristics [15].

A complete organic device model must include bulk charge transport, recombination, space charge, and charge injection, all on the same footing, in order to consistently address all electrical transport data, such as field profiles and transient response as well as J–V curves, at all values of V. This type of model is in principle very general, allowing the effect of varying one parameter, such as the device length, to be examined whilst leaving other parameters unchanged [16–18]. It is a complicated and difficult task to experimentally isolate the effects of varying just one parameter, since barrier heights and mobilities can differ from one device to another, and so systematically testing different device configurations requires considerable care. Methods such as the combinatorial technique, in which a matrix of devices is built on one substrate, have been applied in order to try and overcome this limitation (e.g. [19]).

Because of the differences in charge transport between organic and inorganic semiconductors, the potential difficulty arises that the amorphous nature of organic materials invalidates the assumptions of band transport with electron states that extend throughout the solid, and of a well defined mobility μ. Nevertheless, continuum band models based on semi-phenomenological equations following the concepts of drift and diffusion for bulk transport, and thermionic emission and tunnelling at contacts and interfaces have been successfully applied in modelling OEDs.

Several recent reviews, e.g. [9, 13, 20, 21], have covered the physics of organic electroluminescent devices (OEDs) and of hopping transport in organic semiconductors [22]. In this review, we have focused on the models of transport in OEDs that address its unusual nature and help determine device design. The layout of this review is as follows: section 2 covers continuum band models; hopping transport models are reviewed in section 3; and section 4 provides a brief summary and outlook.

2. Simulations with continuum models

2.1. Introduction to section 2

In this section, we will review the device models from the available literature and will present the equations used to model charge transport in organic LEDs, along with the injection of charge carriers from the electrodes. We will also consider the aspects of device modelling which are unique to OEDs. We will examine the results obtained from the models, and discuss their validity and value. Finally, we will describe some alternative device models that lean away from the inorganic semiconductor framework, and try to provide a more realistic device description.

2.2. Device continuum models

The majority of device models proposed thus far in the literature are based on traditional inorganic charge transport models. Electron and hole transport in the device is described using the continuity equations and a drift–diffusion or drift current, coupled to Poisson's equation. Along with the appropriate boundary conditions, which for OEDs require appropriate formalisms for current injection at each of the contacts, these equations are solved to obtain solutions for the electron and hole current densities, carrier densities, electric field, and electrostatic potential. Owing to the simple device geometry in OEDs, i.e. metal contact/organic layer(s)/metal contact, a one-dimensional device model is generally sufficient.

A variety of models have been proposed, encompassing single-carrier (unipolar) models, double-carrier (bipolar) models, and time-dependent models. Many authors have simplified their models by neglecting the diffusion current contribution, since concentration gradients are generally small. Some models have also been extended to the investigation of multilayer (predominantly bilayer) devices. Multilayer device models use the same equations for current transport and injection, but impose special conditions at the organic–organic interface. These models are discussed below.

2.2.1. Equations defining the model. The time-dependent continuity equations have been used by [23, 24]:

$$\frac{\partial n}{\partial t} - \frac{1}{e}\frac{\partial J_n}{\partial x} = G - R; \qquad \frac{\partial p}{\partial t} + \frac{1}{e}\frac{\partial J_p}{\partial x} = G - R, \tag{1}$$

where J_n (J_p) is the electron (hole) current density, e is the electronic charge, G is the carrier generation rate, and R is the carrier recombination rate. Other authors [17, 25–27] utilize the time-independent versions of these equations in which $\partial n/\partial t$ and $\partial p/\partial t$ are zero. The drift–diffusion current equations are given by the following expressions [17]:

$$J_n = -e\mu_n n\frac{\mathrm{d}\phi_n}{\mathrm{d}x}; \qquad J_p = -e\mu_p p\frac{\mathrm{d}\phi_p}{\mathrm{d}x}, \tag{2}$$

where μ_n (μ_p) is the electron (hole) mobility, n (p) is the electron (hole) density, and ϕ_n (ϕ_p) is the electron (hole) quasi-Fermi potential. The carrier mobilities take the field-dependent Poole–Frenkel form described in section 3 below. J_n and J_p may also be expressed in the following form showing explicitly the drift and diffusion components, in which the diffusivities have been written in terms of the mobilities using the Einstein relation [28]:

$$J_n = e\mu_n\left[nE + \left(\frac{k_BT}{e}\right)\frac{\partial n}{\partial x}\right]; \qquad J_p = e\mu_p\left[pE - \left(\frac{k_BT}{e}\right)\frac{\partial p}{\partial x}\right] \tag{3}$$

where k_B is Boltzmann's constant, E is the electric field, and T is the temperature.

Poisson's equation is

$$\frac{\mathrm{d}E}{\mathrm{d}x} = \left(\frac{e}{\varepsilon}\right)(p - n + N_D - N_A) \tag{4}$$

where ε is the static dielectric constant, N_D is the donor density, and N_A is the acceptor density. The electrostatic potential ψ is related to E by

$$E = -\frac{\mathrm{d}\psi}{\mathrm{d}x}. \tag{5}$$

Using Maxwell–Boltzmann statistics, i.e. assuming that the system is non-degenerate (so far, to our knowledge, OEDs do not exist for which charge densities are so large that this assumption breaks down), n and p are given by

$$\begin{aligned} n &= N_c\exp\{(e\psi - e\phi_n + \chi_c)/(k_BT)\};\\ p &= N_v\exp\{(-e\psi + e\phi_n - \chi_c - E_g)/(k_BT)\}. \end{aligned} \tag{6}$$

N_c (N_v) is the density of states in the conduction (valence) band for an inorganic semiconductor, and here corresponds to the density of negatively (positively) chargeable sites in the film. N_c is often assumed equal to N_v, and determined from the molecular or polymeric density with single occupancy. Here, χ_c is the electron affinity of the semiconductor.

2.2.1a. Traps. The nature of traps in OEDs is widely debated, and there is a variation in their treatment both in analytic calculations and numerical models. It is often argued that the Poole–Frenkel mobility includes shallow trapping of carriers, without needing to explicitly introduce traps. However, deep traps require both an extra recombination term and inclusion of their charge in Poisson's equation. Deep traps may either be described by a discrete (e.g. [17]) or exponential (e.g. [27]) distribution. The trap density is frequently assumed to decay exponentially from the band edge into the band gap and the trapped charge concentrations (n_t for electrons, p_t for holes) are

$$\begin{aligned} n_t &= H_n \exp\{(e\psi + e\phi_n - \Delta_c)/(k_B T_{cn})\}; \\ p_t &= H_p \exp\{(-e\psi - e\phi_n + \Delta_V)/(k_B T_{cp})\} \end{aligned} \tag{7}$$

where H_n and H_p are the electron and hole trap concentrations, and T_{cn} and T_{cp} are the characteristic trap temperatures. In a discrete trap level j, the densities of trapped electrons and holes are given by

$$\begin{aligned} n_t &= \frac{N_{tj}}{[1 + (1/g)\exp\{(E_{tj} - E_{fn})/(k_B T)\}]}; \\ p_t &= \frac{P_{tj}}{[1 + (1/g)\exp\{(E_{fp} - E_{tj})/(k_B T)\}]} \end{aligned} \tag{8}$$

where N_{tj} is the electron trap concentration, E_{tj} is the trap energy, g is the trap degeneracy, E_{fn} is the electron quasi-Fermi level, P_{tj} is the hole trap concentration, and E_{fp} is the hole quasi-Fermi level.

The electron–hole pair recombination rate via traps is calculated using the Shockley–Read–Hall (SRH) model [28]:

$$R_{SRH} = \frac{(np - n_i^2)}{(\tau_{p0}[n + N_C \exp\{-(E_C - E_T)/(k_B T)\}] + \tau_{n0}[p + N_V \exp\{-(E_T - E_V)/(k_B T)\}])} \tag{9}$$

where τ_{n0} and τ_{p0} are the electron and hole recombination times. This trap recombination term must be included in the continuity equations, such that the recombination rate consists of a Langevin recombination rate described below and an SRH recombination rate. Finally, Poisson's equation, expression (4), must be modified by adding the trapped background charge to the right-hand side.

2.2.1b. Recombination and generation in organic materials. For wide-band-gap materials, such as organic semiconductors, carrier generation by thermal excitation across the gap is very small and is usually neglected in calculations. Electron–hole pair recombination in organic semiconductors is bimolecular, taking the Langevin form [16]

$$R_L = \gamma np; \qquad \gamma = 4\pi q \mu_r / \varepsilon \tag{10}$$

where μ_r is an effective mobility which is taken to be the larger of the electron and hole mobilities. Recently, an alternative electron–hole capture mechanism that is more accurate at high fields has been proposed [29].

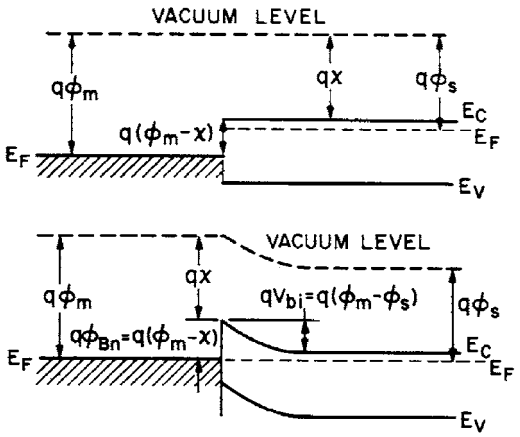

Figure 1. Top panel: the energy band diagram of an isolated metal adjacent to an isolated n-type semiconductor under non-equilibrium conditions. Bottom panel: the energy band diagram of a metal–semiconductor contact in thermal equilibrium (from [87]).

2.2.1c. Contacts. An important aspect of any device simulation is that of the boundary conditions, i.e. the contacts, which are responsible for current injection. The choice of contacts in OEDs is an area of critical importance, as they can affect minority and majority current flow, and hence recombination rates and efficiency. In inorganic semiconductors, such as Si and GaAs, the Schottky energy barrier formed at a metal contact depends weakly on the choice of metal. At the metal–semiconductor interface of an organic semiconductor, there is a much wider variation in the values of the observed barrier height. In fact, the operation of organic LEDs depends on the asymmetry of the barrier heights at the two contacts. ITO is the preferred anode material due to its transparency and relatively high work function. On the other hand, metals such as Al, Ca, and Mg with lower work functions are employed as cathode materials. For a thorough treatment of metal–semiconductor contacts, see [30] and [31]. Although metal–semiconductor contacts are often referred to as Schottky contacts in the literature, this is not the case, and they can be of one of two types: low-resistance ohmic contacts; or rectifying Schottky contacts.

Figure 1 illustrates the formation of a metal–semiconductor Schottky contact (the formation of an ohmic contact is discussed below). Although this discussion is based upon inorganic semiconductor theory, it is applicable since we are discussing band models. As the metal is brought into contact with the n-type semiconductor, thermal equilibrium is established and the Fermi levels in the metal and the semiconductor become continuous and equal through both materials. In order for the Fermi levels to align, electrons from the semiconductor flow into the metal, leaving behind positive ionized donors in the semiconductor. Therefore, the bands bend as shown in figure 1 and a Schottky diode is formed, provided that ϕ_m exceeds the semiconductor work function ϕ_s. If the semiconductor is p-type, electrons are injected from the metal into the semiconductor, causing a build-up of negative charge in the semiconductor, and consequently the bands bend the other way if $\phi_m < \phi_s$. Organic semiconductors have negligible doping and no intrinsic carriers due to the wide band gap, so no band bending occurs. The barrier heights to electron and hole injection, ϕ_{bn} and ϕ_{bp} respectively, can be calculated as follows:

$$e\phi_{bn} = e(\phi_m - \chi_c); \qquad e\phi_{bp} = E_g - e\phi_{bn}. \tag{11}$$

In an OED, the built-in voltage is taken to be the difference between the two metal work functions.

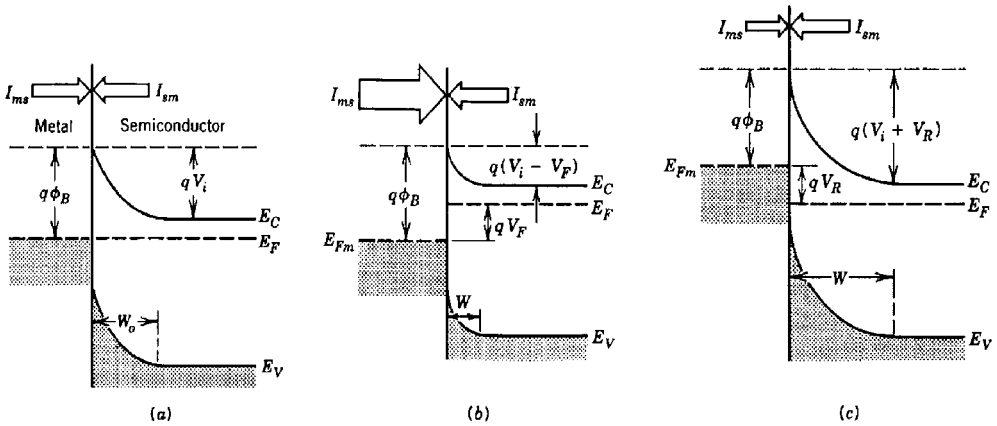

Figure 2. Energy band diagrams of rectifying metal–n-type semiconductor contact at (a) thermal equilibrium, (b) forward bias, and (c) reverse bias (from [88]).

An ohmic contact can also be formed at a metal–semiconductor junction by one of two methods. Firstly, a metal with a work function which is smaller than that of the semiconductor for n-type semiconductors, or greater than that of the semiconductor for p-type semiconductors, can be chosen and no barrier to carrier injection from the metal will be formed. However, this approach is not usually followed because the barrier height may be pinned by the high interface state density at the contact. A more practical method of creating an ohmic contact is to form a Schottky barrier contact, with heavily doped semiconductor at the interface, causing a narrow depletion width, significant band bending, and a barrier which is thin enough to tunnel through.

For most organic semiconductors, increasing the free charge-carrier density through the addition of dopants is difficult to achieve, and so an ohmic contact cannot be formed in this way. It is also difficult to make an ohmic contact via the choice of work function, particularly finding values above typical HOMO levels or below typical LUMO levels. In practice the barrier height is minimized by choosing appropriate contact materials. However, at high biases tunnelling injection does fit experimental data (e.g. [23]), and for low barrier height values (<0.3 eV) SCLC has been observed, which means that contacts which tend towards ohmic behaviour can be fabricated.

Figure 2 shows the conduction band profiles for a metal contact on an n-type semiconductor material in forward and reverse bias. Considering electron flow from the semiconductor to the metal, the potential barrier is reduced and the current I_{ms} (note that the current flows in the opposite direction to the electrons) is increased. However, for electron flow from the metal to the semiconductor, the potential barrier to electrons is independent of the field if image forces are neglected. Therefore, the current for electron flow in this direction I_{sm} is a fixed contribution to the current flow in forward bias, which is matched by I_{ms} at thermal equilibrium.

Under reverse bias conditions, the potential barrier to electrons flowing from the semiconductor to the metal increases, as does the depletion width, and so the current flowing from the metal to the semiconductor I_{ms} is the dominant component. This situation causes a highly asymmetric current–voltage characteristic similar to that of a pn junction diode. However, current flow in Schottky diodes is dominated by majority carriers, whilst in pn junction diodes it is dominated by minority carriers.

Charge transport across the metal–semiconductor interface can be summarized as arising from the following three processes.

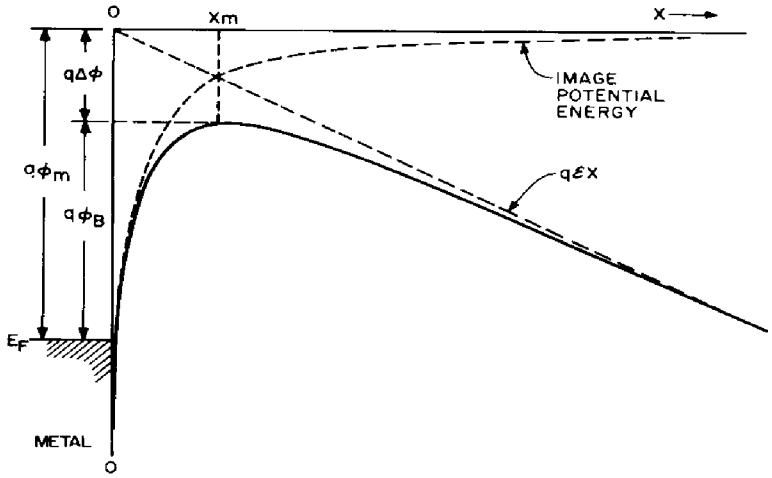

Figure 3. The energy band diagram for the interface between a metal surface and a vacuum. The metal work function is $e\phi_m$. The effective work function (or barrier) is lowered when an electric field is applied to the surface. The lowering is due to the combined effects of the field and the image force (from [30]).

- Transport of carriers from the semiconductor over the potential barrier into the metal. This is the dominant process for moderately doped semiconductors.
- Field emission of carriers through the barrier.
- Recombination in the semiconductor; this corresponds to minority carrier injection.

The heights of the barriers to carrier injection at the contacts for use in simulations are calculated from ϕ_m and the molecular energy levels. However, this assumes that these barrier heights are field independent. In reality, this is not the case. The barrier to injection is reduced under applied bias due to the image force of the carrier, as is illustrated in figure 3. The image force results from the electrostatic attraction of the carrier at a distance x from the electrode–semiconductor interface leading to a charge build-up at the electrode interface that gives the same potential as an equal and opposite charge a distance $-x$ from the electrode, the image charge. The attractive image force is then given by the following expression:

$$E = -\frac{e^2}{16\pi\varepsilon x^2}. \tag{12}$$

The resulting potential energy is

$$U = \frac{e^2}{16\pi\varepsilon x} + eEx. \tag{13}$$

The magnitude of the Schottky barrier lowering, $\Delta\phi_{bn}$, is given by the condition that $\mathrm{d}U/\mathrm{d}x = 0$:

$$\Delta\phi_{bn} = \sqrt{\frac{eE}{4\pi\varepsilon}}. \tag{14}$$

In organic semiconductors, the value of ε is much lower than for inorganic semiconductors, being typically $\approx 3\varepsilon_0$ in organic materials, compared with $12\varepsilon_0$ in Si and $13\varepsilon_0$ in GaAs, increasing the importance of the barrier-lowering term. This contribution must be included for any device model to be successful.

For a heavily doped inorganic semiconductor, or for operation at low temperature, the tunnelling current may be the dominant contact current component. The expressions for J_{ms} and J_{sm} are modified such that they consist of two terms, a thermionic emission term and a field emission or tunnelling term. The thermionic emission current density

$$J_{th} = AT^2 \exp\left\{\frac{-e\phi_{bn}}{(k_B T)}\right\}\left[\exp\left\{\frac{-eV}{(k_B T)}\right\} - 1\right] \tag{15}$$

where A is Richardson's constant. Full expressions for the tunnelling currents in inorganic metal–semiconductor contacts can also be found in [31].

For organic–metal contacts, tunnelling currents calculated using WKB theory or the Fowler–Nordheim [33] formalism are used. In the latter, the electron tunnelling current density,

$$J_{ntun} = \left(\frac{3e^2E^2}{8\pi h\phi_{bn}}\right)\exp\left\{-\frac{8\pi\sqrt{2em_n^*\phi_{bn}^3}}{(3hE)}\right\}, \tag{16}$$

with a similar expression for the hole tunnelling current density J_{ptun}. Here m_n^* is the electron effective mass. However, Fowler–Nordheim tunnelling on its own cannot explain device J–V characteristics when fitted to experimental J–V data [34]. The tunnelling current has been calculated using the WKB approximation in [23], whereas others have used the Fowler–Nordheim formalism (e.g. [17]).

The contacts in a device model are included by describing the carrier currents at the boundaries of the device, $x = 0$ and l, where l is the length of the device. Several types of injecting contact have been used in device models: ohmic, thermionic emission, and tunnelling. Perhaps the most widely used contact injection model was introduced by Davids *et al* [23] and this has been used by numerous other groups (e.g. [35]). In this case, at each contact there are three components to each carrier current. In addition to the tunnelling current and to a thermionic emission component described above, there is a backflowing interface recombination current (the time-reversed version of the thermionic emission process). The thermionic current densities at the contacts can be expressed in terms of effective recombination velocities for electrons and holes, v_{rn} and v_{rp} respectively, so that the total carrier current density at either contact is given by

$$J_n = -ev_{rn}(n - n_{eq}) + J_{ntun}; \qquad J_p = -ev_{rp}(p - p_{eq}) + J_{ptun} \tag{17}$$

where n_{eq} and p_{eq} are the equilibrium carrier densities at the contacts.

In inorganic semiconductors, the carriers are free to propagate into the conduction band with a thermal distribution of kinetic energies. However, in organic materials, the structure is amorphous and conduction occurs via hopping between localized states. The organic recombination velocity was proposed by Scott and Malliaras [36], and is based on the assumption that the recombination is analogous to Langevin bimolecular recombination, and can be considered to be a field-enhanced diffusion process. The organic recombination velocity takes the form

$$v_{rn} = \frac{16\pi\varepsilon(k_B T)^2\mu_n}{e^3}; \qquad v_{rp} = \frac{16\pi\varepsilon(k_B T)^2\mu_p}{e^3}. \tag{18}$$

This results in a substantially reduced recombination velocity compared with that for inorganic semiconductors.

Other authors assume ohmic contacts for simplicity. This assumption is valid provided that the Schottky barrier is small. These boundary conditions were imposed by Shen and Yang [27] by considering large constant charge concentrations at the electrodes. Kawabe *et al* [26, 37] assumed tunnelling injection which they imposed as boundary conditions using the Fowler–Nordheim formalism.

2.2.1d. Organic–organic interfaces. Single layer organic devices tend to be inefficient due to an imbalance of carrier injection and transport. Imbalance from carrier injection is due to the difficulty of obtaining metals with suitable work functions such that the barrier to hole injection at the anode is similar in magnitude to the barrier to electron injection at the cathode. Since ITO is the usual choice of anode, the choice of cathode material is further restricted. This difference in barrier heights usually results in significantly less of one type of charge carrier, the minority charge, being injected than the other. The organic semiconductor materials used to fabricate OEDs tend to be preferentially electron or hole transporters, with the mobility of the faster carrier usually several orders of magnitude higher than that of the other carrier. The imbalance in charge transport means that the carrier population of the slower carrier, generally also the minority carrier, is largest next to its injecting electrode, whereas the majority carrier will be more evenly distributed, and hence much of the recombination will occur close to the minority injecting electrode. This is undesirable since metal electrodes are known to quench excitons, reducing device efficiency. Furthermore, the reduction in the injected minority charge is normally so great that, even allowing for its accumulation near its injecting electrode, recombination is severely limited. Thus, most of the majority carriers will traverse the device without recombining, resulting in a large device current but low efficiency as the ratio of recombination current to device current is low.

A popular and relatively simple method for improving device efficiency is to employ a multilayer structure. A bilayer device can vastly improve performance [5]. Although devices with several layers have been successfully produced, for the purposes of our discussion we shall consider the bilayer case. Such a device improves efficiency by addressing the two main problems associated with single-layer devices, namely imbalanced injection and imbalanced charge transport. Imbalanced injection can be resolved by choosing an appropriate cathode material, resulting in a barrier similar to the barrier between the ITO anode and the other layer. Imbalanced transport is remedied by selecting a hole-transporting layer (HTL) for holes to be injected into the anode, and an electron-transporting layer (ETL) for electrons to be injected into the cathode. An HTL has a higher hole mobility than electron mobility and vice versa for an ETL. Since the HOMO and LUMO levels of the HTL and ETL tend to differ, there is an offset between the bands at the interface. This offset can cause charge build-up and improve the recombination rate and thus efficiency. Materials which present a large barrier at the heterojunction are known as blocking layers.

The use of a blocking layer improves device efficiency, but requires a larger drive voltage, therefore reducing power efficiency. This situation can be improved by using a thinner blocking layer, or even better, a combined blocking and transporting layer, which blocks the majority carrier as before, but also improves transport and possibly injection of the minority carrier, thus balancing injection and transport and increasing both recombination efficiency and power efficiency [16].

It appears that, providing that there are no interfacial chemical reactions, the flat-band condition applies at organic–organic interfaces (i.e. no band bending), and that the band edge offsets that occur between the layers correspond to the band edges in the materials prior to contact formation [32]. In the case of multilayer device models, one approach is the so-called diffusion model, whereby current transport across the heterojunction interface is considered implicitly by simply assuming that the quasi-Fermi levels across the interface are continuous. This approach has been found to provide good results [17]. In order to ensure the accuracy of device models, many authors have explicitly treated current transport across organic–organic interfaces. Assuming an abrupt interface between the two materials, an interface condition for the current can be applied at the heterojunction. A thermionic emission process for current at the interface can be coupled to the drift–diffusion process in the bulk semiconductor [16]. Tunnelling

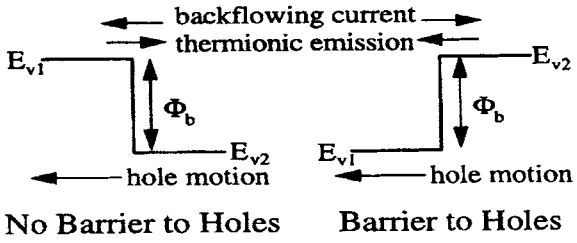

Figure 4. A schematic diagram representing the boundary conditions applied to hole transport at the organic–organic heterojunction (from [16]).

through the band offset has also been applied as an interface condition in the case of inorganic semiconductor heterojunctions, [31], but is deemed to be unnecessary in the case of organic ones. The interface is assumed to be free of sheets of charge, dipoles, and recombination.

Crone *et al* [16] take this type of approach of applying an internal boundary condition for the thermionic emission of carriers over the energy barrier at the organic–organic interface, shown in figure 4. The electrostatic potential, displacement, and carrier current densities are continuous across the interface, and require no special treatment. The drift–diffusion equations at the interface are discretized as a differential equation in the hole density, assuming all other variables are constant across the interface, and integrating across the grid element to obtain the hole density. A similar approach has been implemented by the authors.

Ruhstaller *et al* [39] take a different approach. They use a hopping-type expression for current transport across the energy level discontinuities at an organic–organic interface, which is perhaps more appropriate, as current transport in organic semiconductors is well known as a hopping process. The rate of hopping between two sites differing in energy by δE is given by $\exp\{-(\delta E + E_p)^2/(4k_B T E_p)\}$ where E_p is the polaron binding energy (see [39] and references therein). However, this expression involves the use of an unknown parameter, E_p. Instead, the Miller–Abrahams form for hopping, described in section 3 below, was adopted. The drift–diffusion currents are calculated using average material properties from either side of the interface.

2.3. Applications of device models

As with any semiconductor device model, these models used for simulating OEDs require the input of accurate material parameters, such as density of states, barrier heights, and carrier mobilities, in order to provide useful results. However, unlike the case for inorganic semiconductors, these material parameters are often poorly characterized and are often sample dependent, as a glance through the literature will confirm. Published material parameters usually provide only the starting point for a device model.

In order to obtain good agreement between simulated and experimental data, some fitting of the parameters is usually required. For example, the authors of this review have found that when simulating J–V characteristics to compare to those obtained experimentally, some variation of the barrier height to charge injection, carrier mobility, and field dependence of the mobility is generally required. The values reported in the literature are taken as a starting point and then varied to obtain a best fit to the experimental data. In the case of a unipolar hole-dominated device, the height of the barrier to hole injection at the cathode, ϕ_{bp}, is usually obtained by subtracting the value of the metal work function ϕ_m from the HOMO level of the organic semiconductor. However, it is well known that the work function of ITO, the default

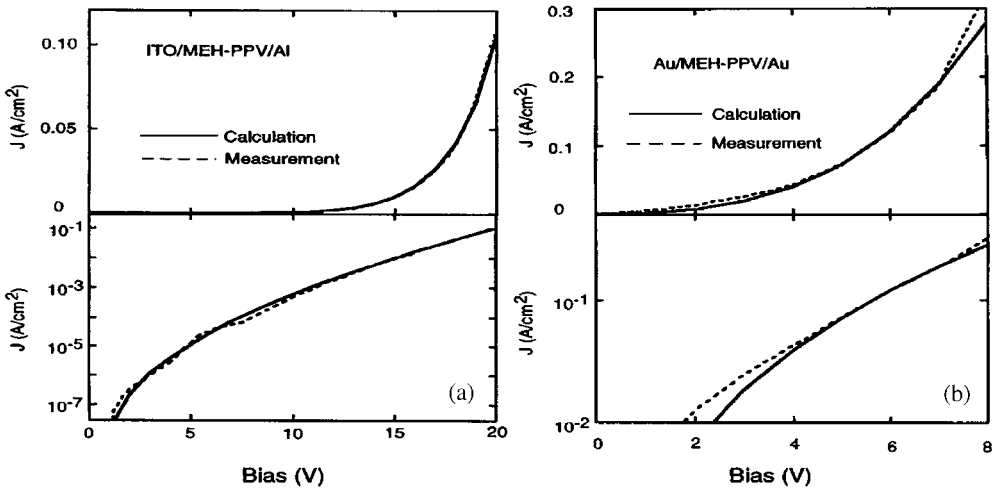

Figure 5. Panel (a): comparison of calculated (solid curve) and measured (dashed curve) current density as a function of applied bias for a 120 nm ITO/MEH-PPV/Al device. Panel (b): comparison of calculated (solid curve) and measured (dashed curve) current density as a function of applied bias for a 110 nm Au/MEH-PPV/Au device (from [23]).

anode material, can vary between 4.7 and 5.2 eV. Hence ϕ_{bp} will vary by as much as 0.5 eV depending on the preparation of the ITO and other factors.

The primary interest in device models has been for use in investigating current flow in OEDs. There has always been debate over the nature of current flow in OEDs, such as whether it is SCLC, injection limited, and so forth. Device models provide a method for investigating such ideas and allow the effects of changing parameters such as barrier heights and carrier mobilities to be examined. We shall now discuss some of the applications of these device models to organic LEDs.

2.3.1. Single-layer device models. The first crop of models were single-layer device models, with either unipolar or bipolar current flow. Such models are more suited to polymer OEDs than small-molecule OEDs, as polymer OEDs, especially initially, tended to be single-layer, e.g. ITO/PPV/Al, devices (e.g. [7]), whereas small-molecule OEDs tend to be bilayer, e.g. TPD/Alq, devices (such as those reported in Tang and VanSlyke [5]).

2.3.1a. Unipolar device models. One of the first device models, by Davids *et al* [23], was used to investigate unipolar current flow. Provided that the barrier to minority carrier injection at the relevant electrode (usually electrons at the cathode) is very large, and coupled with the fact that the minority carrier mobility is usually orders of magnitude lower than that of the majority carrier, then the assumption of unipolar current flow is valid. This type of model is useful for trying to investigate current flow in single-layer devices and to examine in the case of injection-limited current flow what type of injection expression is appropriate. The obvious drawback of such a model is that it ignores carrier recombination, a vital component of any organic LED model.

Davids *et al* [23] found that many single-layer devices could be approximated as just single-carrier current devices, owing to the presence of a larger minority carrier barrier. As can be seen in figure 5, their model provided fairly good fits to experimental J–V data for

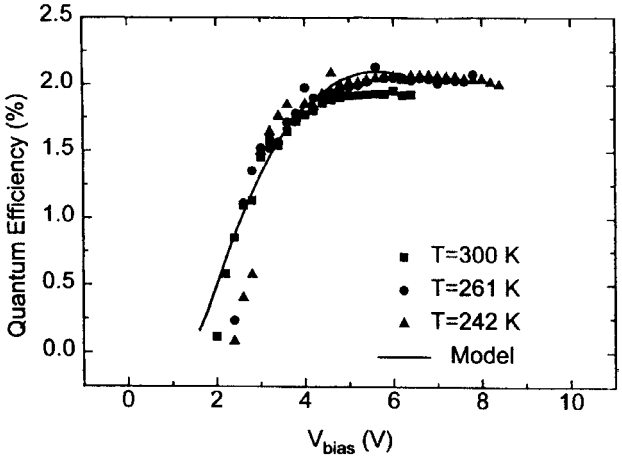

Figure 6. External quantum efficiency (photons/carrier) versus applied bias for a 110 nm ITO/PPV/Ca device at temperatures of 242, 261, and 300 K (from [41]).

devices such as ITO/MEH-PPV/Al and Au/MEH-PPV/Au. They observed both SCLC and injection-limited current flow, and concluded that for Schottky barriers to majority carrier injection (holes) of up to 0.3–0.4 eV, the current flow was space-charge limited, whilst for larger values it was injection limited. They also noted that for the device with the larger barrier to hole injection (ITO/MEH-PPV/Al), which had injection-limited current, the hole density and electric field were highly uniform across the device, whereas for the device with the lower barrier to hole injection case (Au/MEH-PPV/Au), the hole density and field were highly non-uniform.

2.3.1b. Bipolar device models. Clearly, a more realistic device model must incorporate both charge carriers and their recombination. Bipolar models allow the recombination and internal quantum efficiencies to be calculated, as well as illustrating recombination zones within a device, both of which are clearly of use when attempting to improve device efficiency. Analytic expressions for current flow in bipolar devices are invalid, e.g. child's law for SCLC, or do not exist, making models useful for analysing data.

The recombination current density, J_r, for a device of length L can be written as [16]

$$J_r = \int_0^L qR\,\mathrm{d}x = J_n(0) - J_n(L) = J_p(0) - J_p(L). \tag{19}$$

Holes injected at $x = 0$ either recombine in the device and contribute to J_r or traverse the device and contribute to $J_p(L)$. A similar situation exists for electrons. If more carriers reach their collecting electrode, the J_r is reduced and hence also the recombination efficiency η_r. In terms of the total current density $J = J_n + J_p$,

$$\eta_r = J_r/|J|. \tag{20}$$

The internal quantum efficiency is then given by

$$\eta_q = Q\eta_r. \tag{21}$$

According to spin statistics, the ratio of non-radiative triplets formed to radiative singlets is 3:1, so $Q = 1/4$.

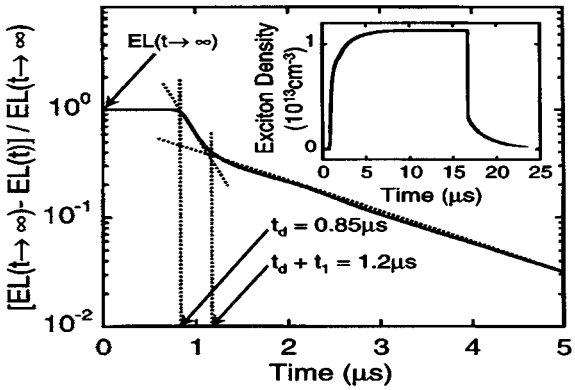

Figure 7. A plot of the simulated final magnitude of the (normalized) EL minus the EL at time t as a function of time for a PPV-like device, showing how t_d and t_1 are calculated. The inset shows the simulated response of the exciton density for a PPV-like device to a square voltage pulse ($V - V_{bi} = 5$ V) (from [35]).

Blom and de Jong [41, 42] modelled J–V data for an ITO/PPV/Au and an ITO/PPV/Ca device. As well as obtaining good fits to their experimental data using the model, they also investigated recombination in their devices and these results are shown in figure 6. They concluded that to improve device efficiency, the fraction of non-radiative recombination events needed to be reduced and that using an electron-transporting/emissive layer could help improve efficiency by moving the recombination zone away from the potentially quenching metallic cathode.

Martin *et al* [18] used a bipolar drift–diffusion model to interpret J–V and efficiency data for an ITO/MEH-PPV/Al device over a range of temperatures. This device was similar to the device whose J–V characteristics were measured and modelled by Lupton and Samuel [25, 40]. In [25, 40], the model was unipolar and only considered drift current. Good agreement was obtained with experimental data by varying the barrier to hole injection, the zero-field mobility, and the field dependence of the mobility fitted to the Poole–Frenkel form, especially at high fields and high temperatures. However, the difficulty experienced by the authors of [18] in explaining the observed temperature gradients of the hole and electron barrier heights suggests that more work needs to be carried out in understanding injection into organic devices. The model predicted a reduction in efficiency as the temperature increases, in agreement with the experimental results. This effect arises from the increases in the barrier heights to electron and hole injection, ϕ_{bn} and ϕ_{bp}, which outweigh the increase in carrier mobilities. In practice, although not in the model, a further reduction in efficiency may come from the more rapid increase in hole mobility than electron mobility with temperature, leading to less balanced transport.

Others [17, 24, 26, 27, 35, 43, 44] have used bipolar models to investigate single-layer device characteristics using organic material parameters. One of the most important results, which has been shown by many of these authors, is that of the need for charge balance in the single-layer devices in order to maximize efficiency, and that the minority carrier determines the recombination rate. Ideally, both charge injection and transport should be balanced, although this is often difficult to achieve with single-layer devices.

Pinner *et al* [35] used their time-dependent model to investigate the behaviour of OEDs when subjected to a pulsed excitation. Specifically, as illustrated in figure 7, they used their model to compare the transient electroluminescence of an OED to that measured experimentally. In this way, they showed how electroluminescence evolves with time after

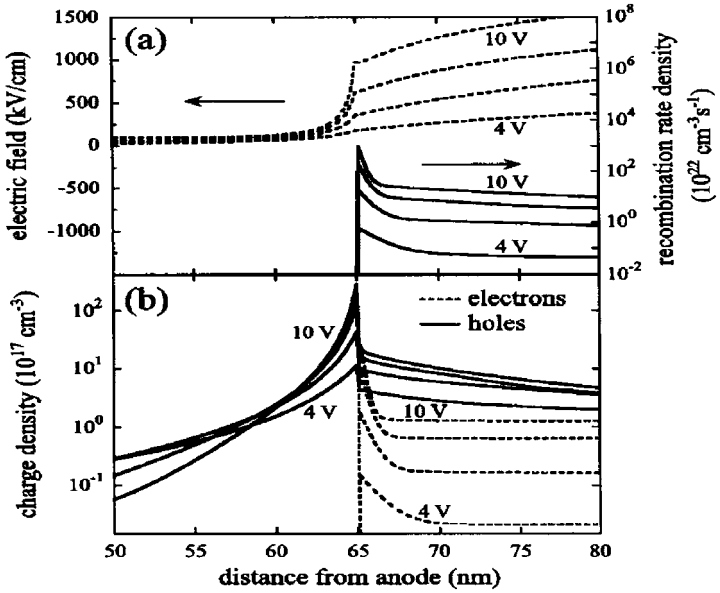

Figure 8. Top panel: the electric field and recombination rate density and bottom panel: the charge density distribution in a bilayer TPD (65 nm)/Alq (50 nm) device, with a 0.5 eV cathode barrier, at applied biases of 4, 6, 8, 10 V. As the bias is increased, the confinement of holes to the internal interface is enhanced, causing the electric field ratio from Alq to TPD to increase. Similarly, the electron pile-up on the Alq side narrows with increasing bias, resulting in enhanced confinement of the recombination rate density (from [39]).

being subjected to a step voltage pulse. This technique yields information such as current heating effects and charge storage in the OED, and allows determination of carrier mobilities. Its advantage is that it allows access to higher-field regimes where, under constant-bias conditions, devices may fail.

2.3.1c. Multilayer device models. There has been a lot of interest in multilayer, especially bilayer, devices, and hence there is a natural progression to device models able to simulate such devices. As has been previously noted, single-layer devices in which carrier mobilities and injection rates are unequal have carrier recombination localized near the electrode which injects the minority carrier. The recombination peak can be moved away from the electrodes by using a second blocking layer, which prevents the majority carrier from reaching the other electrode [16]. Such behaviour has also been seen in the model of Blades and Walker [17].

Scott *et al* [45] extended their model to allow the simulation of multilayer devices, using the approach detailed previously. In the paper by Ruhstaller *et al* [39], they use this model to investigate the steady-state operation of bilayer OEDs (example results are given in figure 8) and transient electroluminescence of bilayer devices, and they investigate the potential benefits of some artificial three-layer devices.

Martin *et al* [46] have used a drift–diffusion model to simulate bilayer structures in which the average electric field values in a bilayer NPB/Alq device obtained experimentally by electroabsorption (EA) spectroscopy were compared to those obtained from the simulation. As well as obtaining good agreement with the experimental data, as can be seen from figure 9, the model allowed us to interpret the results. The average field in a particular layer of the device depends critically upon the barrier to carrier injection into a layer, and whether the other layer

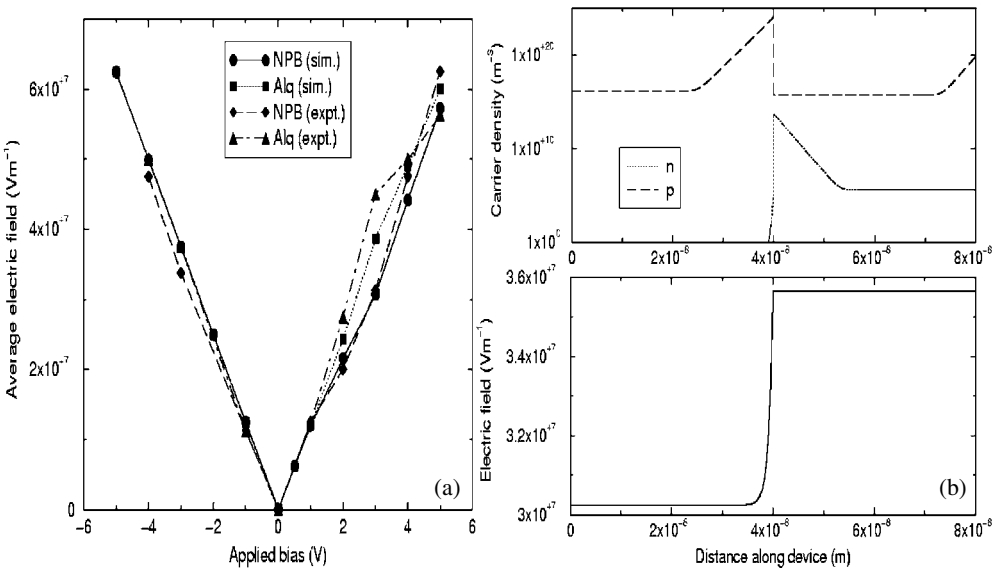

Figure 9. Panel (a): experimentally measured (by EA spectroscopy) and simulated average electric field values in an ITO/NPB(40 nm)/Alq(40 nm)/Al device. Panel (b): electric field profiles and carrier density profiles for this device for an applied bias of +4 V (from [46]).

acts as a blocking layer to that carrier. For example, in the case of an ITO/NPB/Alq/Al device, the barrier to electron injection at the Alq/Al interface is very large and relatively small numbers of electrons are injected. However, the barrier to hole injection at the ITO/NPB interface is much smaller and large numbers of holes are injected. The NPB is an efficient hole transporter, but the Alq layer acts as a hole blocking layer. Holes accumulate at the internal NPB/Alq interface, and, applying Poisson's equation, the field across the Alq layer is found to be fairly constant and significantly larger than the field in the NPB layer. In the case of an ITO/NPB/Alq/Al:Li device, the results are somewhat different, but still excellent agreement is obtained between theory and experiment. As before, holes are injected into the NPB and accumulate at the NPB/Alq interface. However, the Al:Li electrode has a lower work function than Al and so electrons are injected into the Alq layer. The Alq is an efficient electron-transporting material, but the NPB acts as an electron blocking layer, and so electrons accumulate at the NPB/Alq layer, but on the opposite side to the holes, in the Alq. NPB blocks electrons more effectively than Alq blocks holes, so there is a larger electron density than hole density at the interface, which according to Poisson's equation results in a larger field throughout the NPB layer than the Alq layer.

A TPD/Alq bilayer device was modelled by Martin and Walker [47] with the aim of finding the Alq layer thickness that optimized the optical recombination rate. Their result agreed with the optimum thickness measured using a combinatorial technique [19]. Here, a matrix of 49 OEDs with different configurations and layer thicknesses was set up on a single substrate. Efficiency plots for all the OEDs were simultaneously measured. Thus a single parameter could be varied, keeping others constant. Agreement between the theory in [47] and experiment was encouraging, given that the parameters used in the bilayer model were taken from the literature.

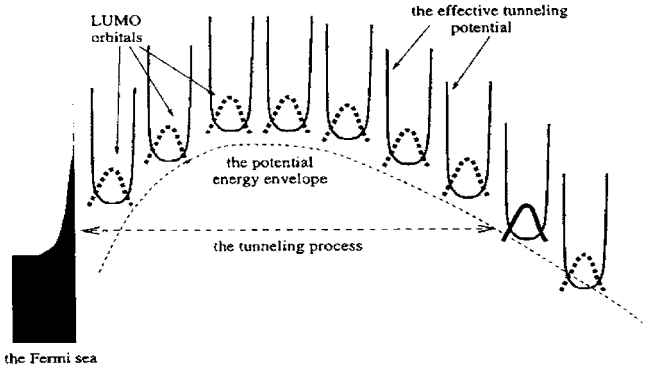

Figure 10. A schematic diagram showing tunnelling injection. The energy is shown as a function of the position within the organic layer (from [49]).

2.4. Alternative numerical models.

Although the drift–diffusion device models have been popular, attempts have been made to create models which include the disorder in the materials and the mechanisms of charge injection and transport between molecular sites. Tutiš *et al* [48, 49] have proposed a numerical model which contains a detailed description of contacts, charge transport, and recombination, pertaining to the details of organic semiconductors and OED structures. They have presented a one-dimensional model in which the electrons and holes are confined to discrete points, which represent molecules. At each node in the simulation (a node represents a molecular site), the electron and hole densities, as well as the energy levels (i.e. HOMO and LUMO levels), are calculated as shown in figure 10. The charge density then evolves at each site over time according to contributions from carrier injection, transport and recombination.

The energies of the HOMO and LUMO levels vary throughout the device according to the type of organic molecule being described at a node, and according to electric field and space-charge effects. The energy of a local LUMO level at site x is given by

$$\bar{E}(x) = E_0 + E_{IF} + \sum_m E(x_m, x) \tag{22}$$

where E_0 is the bare LUMO energy, E_{IF} is the image force contribution due to the metal electrodes, and $E(x_m, x)$ is the contribution of charge at node x_m. A similar equation can be written for the energy of the HOMO levels. The variations of the electron and hole densities at a node, n_m and p_m respectively, over time have three contributions: charge injection from the electrodes (inj), transport between sites ($tran$), and recombination (rec)

$$\begin{aligned} \frac{\mathrm{d}n_m}{\mathrm{d}t} &= \left(\frac{\mathrm{d}n_m}{\mathrm{d}t}\right)_{inj} + \left(\frac{\mathrm{d}n_m}{\mathrm{d}t}\right)_{tran} + \left(\frac{\mathrm{d}n_m}{\mathrm{d}t}\right)_{rec}; \\ \frac{\mathrm{d}p_m}{\mathrm{d}t} &= \left(\frac{\mathrm{d}p_m}{\mathrm{d}t}\right)_{inj} + \left(\frac{\mathrm{d}p_m}{\mathrm{d}t}\right)_{tran} + \left(\frac{\mathrm{d}p_m}{\mathrm{d}t}\right)_{rec}. \end{aligned} \tag{23}$$

Carrier injection occurs via tunnelling of carriers from the metal electrodes to near nodes. Transport of carriers within the material occurs by nearest-neighbour hopping, and recombination is assumed to have the Langevin form. Transport across the organic–organic interface in a multilayer device is performed by intersite hopping in a manner similar to that operative for charge transport within one organic layer.

A rather different approach to continuum modelling of OEDs was taken by Davids *et al* [50] who developed a device model based on the non-degenerate continuum model of Brazowskii

and Kirova for the electronic structure of polymers, in which polarons and bipolarons are the principal charged excitations. This model was found useful in interpreting capacitance–voltage and EA measurements. The former demonstrated that the OEDs are fully depleted and enabled deduction of trap densities, and the latter allow deduction of effective Schottky barrier heights.

2.5. Transport models with optical modelling

The overall thickness of the device at a few hundred nanometres is comparable to the optical path lengths for the emission wavelengths used in these structures. Hence, significant optical interference effects are to be expected, especially affecting blue emission. Device models capable of optimizing the external quantum efficiencies need to be able to include these effects, which can be done either within the approach of Crawford [51] or Chance *et al* [52].

Staudigel *et al* [53] presented a model based on a similar principle to that of Tutiš *et al* [48, 49]. Again, the device under examination was considered to be one dimensional, as a stack of discrete molecules. Their model includes space-charge effects, charge-carrier drift and diffusion, injection, bulk recombination, and trapping. They also included singlet exciton diffusion and decay. Charge-carrier drift and diffusion are incorporated by carriers hopping between sites, with the carrier drift depending on the local electric field, whereas the carrier diffusion is represented as a random movement due to thermally stimulated hopping processes with no preferential direction. Carrier injection in the model is taken care of by assuming ohmic contacts—this is implemented by having a large number of charge carriers waiting at the organic–electrode interfaces. Electron–hole pair recombination in the bulk is again implemented as a Langevin-type recombination, which is due to coulombic interaction between the two carriers.

Trap states are treated as energy levels which exist between the HOMO and LUMO levels. The traps are neutral when empty, and their occupation depends on the free charge-carrier densities and the trap depth. For shallow trap states (trap states arising from structural disorder in the materials) recombination between trapped charge and free charge is assumed to be radiative with the same efficiency as recombination between pairs of free charge carriers. Internal organic–organic interfaces are treated by assuming that a carrier at the interface can move in one of only two ways. It can either perform a thermally assisted jump over the energy barrier at the interface, or recombine with a free carrier from the other side of the interface. In the model, the recombination of electrons and holes is assumed to create singlet and triplet excitons in the ratio 1:3 in accordance with spin statistics. The change in singlet exciton density at a point in the device during a time step is due to formation and decay, diffusion, and non-radiative decay caused by quenching by either the electrodes or free charge carriers.

Several authors [35, 39, 44] have incorporated the density of singlet, i.e. radiative, excitons, S, into their models, by including their generation, diffusion, and decay. Models which only include the generation rate indicate the recombination zone, but this may be different to the emission zone for the reasons given above. The singlet exciton continuity equation is given by

$$\frac{\partial S}{\partial t} = f_{ex} R_L(x,t) + \frac{\partial}{\partial x}\left[D_S \frac{\partial S}{\partial x} \right] - \frac{S(x,t)}{\tau_{ex}} = 0 \tag{24}$$

where f_{ex} is the fraction of singlet excitons generated (assumed to be $1/4$ according to spin statistics); D_s is the diffusion constant given by L_{ex}^2/τ_{ex}, where L_{ex} is the diffusion length and τ_{ex} is the exciton lifetime. Effects which may cause non-radiative decay of excitons—quenching by electrodes, defects, and so forth—are ignored. Tessler [44] has used the optical model developed by Chance *et al* [52] to calculate the exciton decay rate in equation (24). Such combined optical/charge transport models would appear to be very desirable in designing

devices that emit radiation efficiently, since coupling of the excitons to photon states is strongly affected by the device geometry. In typical OED structures, the metallic cathode acts as a mirror, which modifies the pattern of the electromagnetic modes near the cathode, setting up standing wave states [52]. By causing energy transfer into the metal plasmon modes, this alters the radiative emission [54, 55]. The exciton–photon coupling can however be exploited in microcavity devices which produce spectral narrowing [56] and are capable of supporting optically pumped lasing [57].

3. Simulations of hopping transport

3.1. Introduction to section 3

There are two explanations for conduction in organic materials, which while conceptually different, lead to predictions that are often hard to distinguish experimentally. The first explanation, known as the multiple-trapping model, has already been described in section 2. In this model, transport of a carrier via extended states is repeatedly interrupted by trapping in localized states. In the second explanation, reviewed in this section, the carriers hop directly between the localized states. This approach is motivated by the fact that many (though not all—see e.g. [58]) time-of-flight (TOF) measurements have shown that the dependence of the mobility μ on the electric field E is approximately of the Poole–Frenkel form for many OEDs, for which

$$\mu = \mu_0 \exp\{\sqrt{E/E_0}\}, \tag{25}$$

where μ_0 is the zero-field mobility for a particular carrier species in the material and E_0 is a constant for a given material that is temperature dependent. This field and temperature dependence has been found to fit the following form [59]:

$$\mu_0 = C \exp[\Delta/(k_B T)], \qquad \frac{1}{E_0} = B\left[\frac{1}{k_B T} - \frac{1}{k_B T_0}\right] \tag{26}$$

where C, Δ, T_0, and B are material constants related to the degree of disorder in the material. Poole and Frenkel predicted that in doped inorganic semiconductors, μ has a similar variation with field and temperature, varying as $\exp\{-(E_C 2e^{3/2}E^{1/2}/(\varepsilon^{3/2}k_B T))\}$ where E_C is the conduction band edge, due to a reduction of the donor ionization energy in a field E [60]. This explanation is not valid for OEDs, as dopant concentrations are generally low.

In this section, we review the hopping transport models and show how they can predict the Poole–Frenkel mobility over at least some range of fields. These models all use the Monte Carlo technique where random numbers are employed to determine the outcome of several possible moves. Section 3.2 explains the Gaussian disorder model (GDM) and its variants, and in section 3.3 we show how it has been applied to the study of charge transport in OEDs. Section 3.4 addresses Monte Carlo simulations of the relaxation and dissociation of excitons.

3.1.1. Dispersive transport. In amorphous materials, transport is frequently referred to as dispersive. As noted by Scott *et al* [61], this term has four meanings. Firstly, it has the rather vague meaning of transport in which the mean velocity decreases with time. Secondly, it can refer to the fact that no shoulder is visible on a linear plot of current I versus time t, but on a $\log(I)$–$\log(t)$ plot does have a clearly defined shoulder from which a transit time may be deduced. Thirdly, the term dispersive is used in the context of models in which each charge resides for a time, the waiting time, before hopping to a nearby site. The transition time for between sites is assumed to be short compared to the hopping time. Such models are commonly used to describe transport in amorphous systems, the archetype being that of Scher

and Montroll [62]. Finally, dispersive transport is defined as that in which all $I(t)$ plots show a universal character in that they lie on top of each other regardless of sample thickness and field. Thus the width and all other moments of the carrier packet increase at the same rate as its mean displacement. This behaviour is seen in the Scher–Montroll model [62]. In [61], it is argued that transport in OLEDs is dispersive in some aspects but not all.

Marshall [11] has also provided a review of anomalous dispersion, which is akin to the dispersive transport mentioned in the previous paragraph, and discussed how it shows up in models based on both multiple trapping and hopping transport. He has pointed out that Pollak [63] noted a key difficulty with seeing anomalous dispersion in hopping models, namely that sites which have long release time constants necessarily possess a low entry probability.

3.2. The Gaussian disorder model

Much theoretical work has been done investigating the mobilities of organic molecular systems within the framework of the GDM [64]. Non-crystalline organic solids, such as molecularly doped crystals, molecular glasses, and conjugated polymers, are characterized by small mean free paths for the charge carriers, as a result of the high degree of disorder present in the system. Therefore, the elementary transport step is the charge transfer between adjacent transporting elements, which can either be molecules participating in transport or segments of a polymer separated by topological defects. These charge-transporting elements are identified as sites whose energies are subject to a Gaussian distribution

$$\rho(\varepsilon) = (2\pi\sigma^2)^{-1/2} \exp\{-\varepsilon^2/(2\sigma^2)\} \tag{27}$$

where the energy ε is measured relative to the centre of the density of states. Within this distribution, all states are localized. The choice of such a distribution was based on the Gaussian profile of the excitonic absorption band, as well as on the recognition that the polarization energy is determined by a large number of internal coordinates which vary randomly by a small amount, so the central limit theorem of statistics holds.

In this model, the jump rate between two transporting sites i and j is assumed to be of the Miller–Abrahams type:

$$\nu_{ij} = \nu_0 \exp\{-2\gamma R_{ij}\} \begin{cases} \exp\{-(\varepsilon_j - \varepsilon_i)/(k_B T)\}, & \varepsilon_j > \varepsilon_i \\ 1, & \varepsilon_j < \varepsilon_i \end{cases} \tag{28}$$

where R_{ij} is the intersite distance. When a field E is applied, the site energies also include the electrostatic energy. In addition to the energetic disorder of the transporting sites, geometric disorder can also be taken into account by allowing separate site-specific contributions in the overlap parameter $2\gamma = \Gamma_i + \Gamma_j$ to be subjected, in a similar fashion, to a Gaussian distribution of variance Σ (off-diagonal disorder). In this way, local variations in intersite distance and in mutual molecular orientations can be taken into account.

The above model has been treated by the Monte Carlo simulation technique, in which charge transport is described as an incoherent random walk. The carriers start their motion from randomly chosen sites at one of the boundaries of the system sample. Their trajectories are specified from the constraint that the probability for the carriers to jump between two transporting sites is

$$p_{ij} = \frac{\nu_{ij}}{\sum_{i \neq j} \nu_{ij}}. \tag{29}$$

With this technique, TOF measurements can be simulated, in which μ is derived from the mean arrival time of the carriers at the other end of the sample and from their mean displacement. The predictions made with this model concern the temperature and field dependence of the

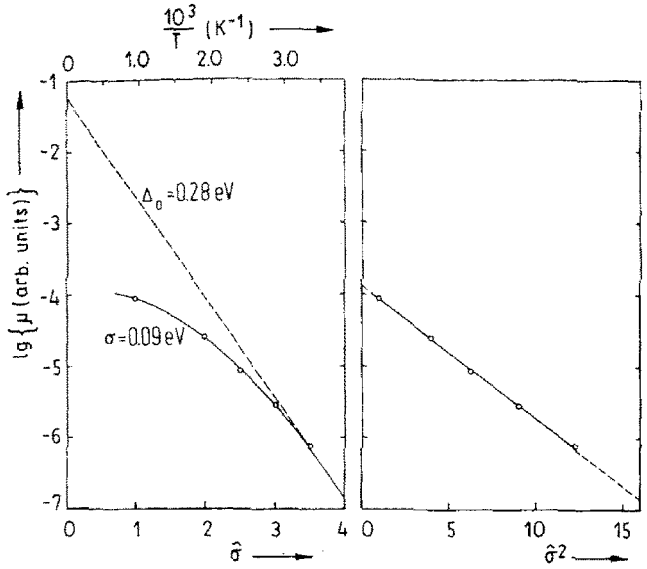

Figure 11. A log–linear plot of low-field μ as a function of $\hat{\sigma}$ (left panel) and $\hat{\sigma}^2$ (right panel) where $\hat{\sigma} = \sigma/(k_B T)$ is the degree of energetic disorder. The straight line in the left panel shows an Arrhenius fit chosen to match the data around 300 K (from [64]).

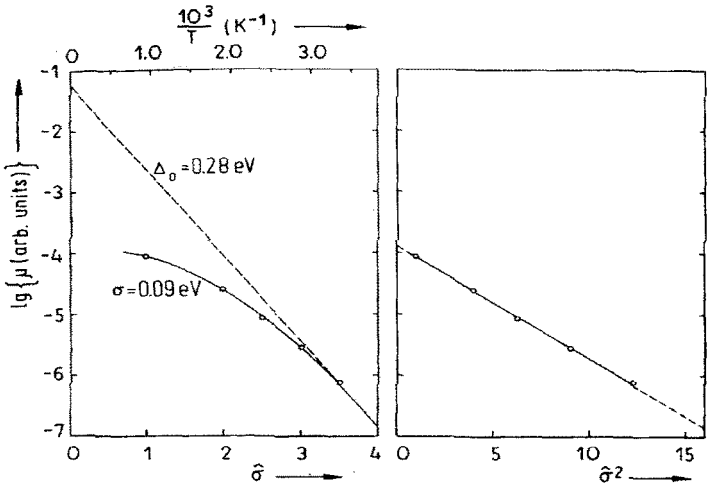

Figure 12. μ versus $E^{1/2}$ (E in MV cm^{-1}), for different values of $\hat{\sigma}$ (from [64]).

charge-carrier mobility of molecularly doped materials. In particular, at low fields, $\ln(\mu)$ has been shown to have a temperature dependence of the form $1/T^2$ rather than $1/T$, as is seen in figure 11.

The interplay between energetic and positional disorder has been investigated for a range of electric fields and different temperatures. When a system is subject to energetic disorder only, μ is initially approximately constant for low fields, and increases as we increase E (figure 12). This enhancement of the mobility for strong fields is the result of the fact that larger fields decrease the activation energy for forward jumps, enabling the motion of the charge carriers.

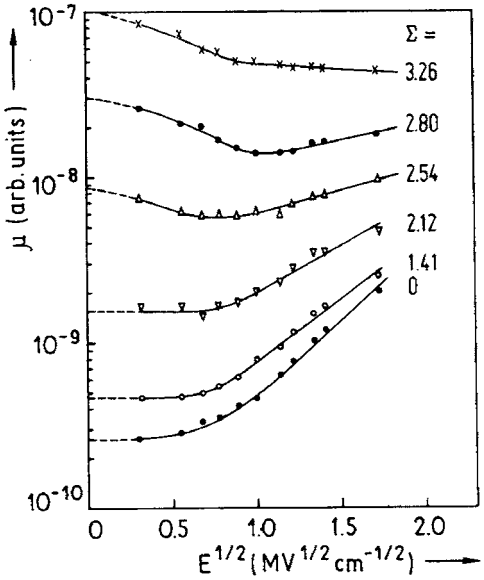

Figure 13. As for figure 14, but for fixed $\hat{\sigma} = 3$ and different values of off-diagonal disorder Σ (from [64]).

However, at high enough fields the mobility must saturate since the gain in the electrostatic energy overcompensates the activation energy due to disorder. A consequence of this saturation is the decrease in μ at very large fields for diminishing disorder. The $\ln(\mu) \propto E^{1/2}$ dependence is observed, albeit within a limited range of electric fields. On the other hand, for a system that is governed only by positional (off-diagonal) disorder, figure 13 shows that increasing E for small disorder yields mobilities that increase. A larger degree of disorder, however, tends to create more traps for the hopping carrier, which it can only overcome by moving against the direction of the electric field. Thus, increasing E reduces μ. The influence of both energetic and geometric disorder is seen from a change in the slope of $\ln(\mu)$ versus $E^{1/2}$ from positive to negative for increasing Σ. With both types of disorder, μ can be described by the approximate formulation

$$\mu(E,T) = \mu_0 \exp\{-4\hat{\sigma}^2/9\} \begin{cases} \exp\{C(\hat{\sigma}^2 - \Sigma^2)\sqrt{E}\} & \Sigma \geqslant 1.5; \\ \exp\{C(\hat{\sigma}^2 - 2.25)\sqrt{E}\} & \Sigma < 1.5, \end{cases} \tag{30}$$

where $\hat{\sigma}$ is $\sigma/(k_B T)$, C is an empirical constant, and the mobility factor μ_0 is a function of concentration.

3.2.1. Variations of the Gaussian disorder model.

3.2.1a. Geometric disorder. In the case of geometric (off-diagonal) disorder for the hopping model described in section 3.1, the strength of electronic coupling among sites is split into separate contributions from the relevant sites, each obtained from a Gaussian probability density. However, the choice for the off-diagonal disorder of a Gaussian distribution is not theoretically sustained unlike in the case of energetic disorder, and a more realistic way of representing geometric disorder has been pursued. One such attempt is described in [65], in which an alternative approach comprising positional and orientational disorder is introduced via

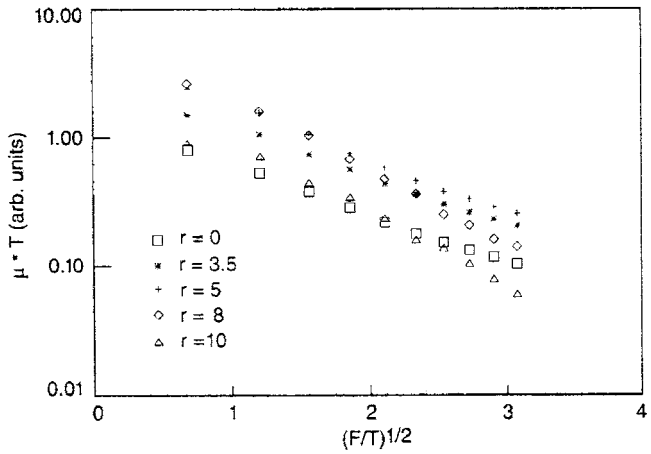

Figure 14. μT versus $F/T = [eEa/(k_B T)]^{1/2}$ where a is the distance between nearest-neighbour sites for diagonal disorder parameter $\sigma = 0$ and different values of r (the variable specifying minimum and maximum values for ξ_{ij} and hence the extent of off-diagonal disorder). If $a = 0.9$ nm, $F = 100$ K gives $E = 10^5$ V cm^{-1} (from [65]).

fluctuations in the bonds adjoining the various transport sites rather than site fluctuations. This model gets rid of the unnecessary correlations between hops, which characterize the Gaussian disorder model in section 3.1, and result in overestimating the contribution of longer hops.

In particular, Gartstein and Conwell [65] performed Monte Carlo simulations of hopping with the elementary jump rate described by equation (28), but in which

$$W_{ij} = \exp(\xi_{ij}) \exp(-2\gamma r_{ij}), \qquad -r \leqslant \xi_{ij} \leqslant r \tag{31}$$

where ξ_{ij} is a uniformly distributed random variable which refers to the bonds. In this way, the different bonds of a given site with its neighbours are uncorrelated. Within this framework for off-diagonal disorder, the behaviour of the mobility was investigated for various regimes of the electric field. In figure 14, the mobility is seen to decrease monotonically with E. In the low-field regime, low off-diagonal disorder gives rise to a smaller mobility than for higher disorder, since the disorder can produce a larger number of favourable jumps. However, increasing the field will eventually cause the mobility to saturate, no matter how strong the disorder is. Comparison with the mobility obtained from the Gaussian disorder model shows agreement between the two approaches with respect to the monotonic decrease of the mobility. Nevertheless, the GDM predicts that stronger off-diagonal disorder would result in larger changes of μ, especially in the low-field regime. This difference was attributed to the presence of more favourable paths for the charge carrier in the GDM due to the unscaled contribution of longer paths. The disagreement becomes more pronounced when both energetic and geometric disorder are included in the simulations. Even though the disorder model shows that the mobility increases in a monotonic way with respect to increasing off-diagonal disorder, for all electric field ranges examined, the approach by Gartstein and Conwell [65] shows (figure 15) that at all fields, the mobility increases with the field for low values of off-diagonal disorder. On the other hand, as the disorder becomes stronger as specified by the parameter r, μ decreases with the field.

An important point that was also stressed was that different forms of off-diagonal disorder give different predictions for the mobility in the region of increased fields. For example,

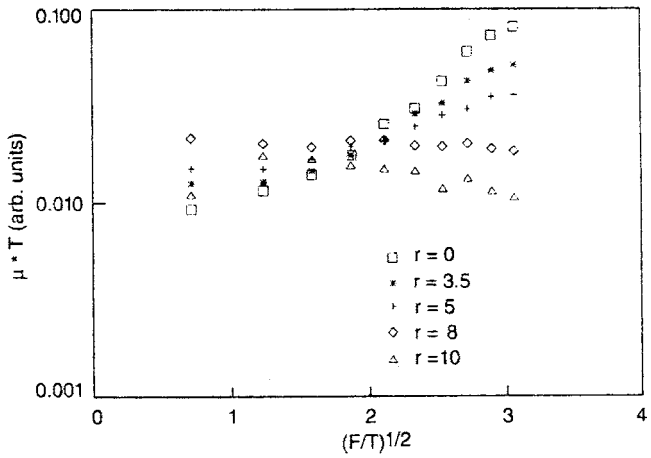

Figure 15. As for figure 14, but with $\hat{\sigma} = 3$. Reprinted with permission (from [65]).

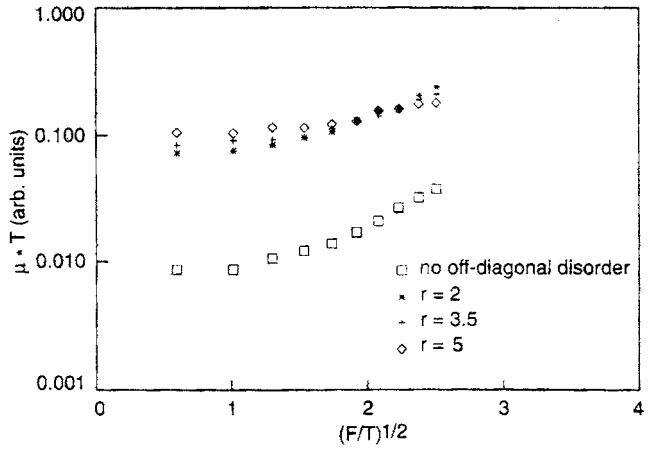

Figure 16. As for figure 14, but with ξ'_{ij} in the range exp(−3) to exp(3) (from [65]).

examination of a more uniform distribution of the geometric disorder where

$$W_{ij} = \xi'_{ij} \exp(\xi_{ij}) \exp(-2\gamma r_{ij}) \tag{32}$$

exhibits a weaker field dependence for μ (figure 16) than is seen in figure 15. Despite the fact that for a Miller–Abrahams jump rate, the variation of μ with E is independent of disorder in the ohmic and saturation regimes, the location of those regimes and the dependence of μ on the electric field in the intermediate-field regime depend on the details of the model assumed. This calls for more realistic distributions.

Another approach for the description of positional disorder was presented by Hartenstein *et al* [66], and was based on Monte Carlo simulations of transport on a dilute lattice. This treatment employs the GDM, but without the need for defining a distribution function for the electronic coupling between different sites. In this case the hopping sites having nearest neighbours were grouped as clusters whose size depends on the fixed concentration c of transport sites. Electronic coupling depends on the random intercluster distances, but ignores any contribution from the random orientation of the transporting elements. Nevertheless, the

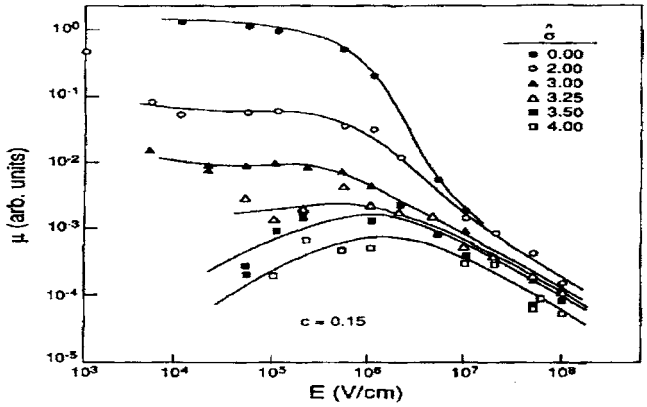

Figure 17. μ versus E (E in V cm^{-1}), for different values of $\hat{\sigma}$ for fixed $c = 0.15$ (from [66]).

model is adequate for low dopant concentrations for which there are large fluctuations in the intersite distances. Predictions of the mobility shown in figure 17 demonstrate the same temperature dependence as that of equation (30), i.e. at large values of $\hat{\sigma}$, μ has a maximum followed by $\mu \propto E^{-1}$, the latter being characteristic of the high-field regime. There are some differences, however, between the dilute and the non-dilute cases. In the dilute case, when both diagonal and off-diagonal disorder are retained, the field range for which there is saturation of the mobility is smaller than for an undiluted system. Also, the $\ln(\mu)$ versus $\ln(E)$ curves appear smoother in the former situation, with a more extended region of electric fields for which the change of the sign of the slope from positive to negative occurs.

The strength of the above model has been demonstrated by comparison of the results it provides with experimental measurements. However, in order to be able to account for all systems examined, an extra modification was required; specifically, the term $\exp(-\Delta/k_BT)$ should multiply μ_0 on the right-hand side of equation (30). This term corresponds to the inclusion of a constant activation energy Δ. Simulation results for the field dependence of the mobility are in reasonable agreement with the experimental findings as seen in figure 18, despite the assumptions required for the statistics of the intersite distances. Since the asymptotic high-field behaviour of μ is captured by this disorder model for dilute systems, it looks a promising formalism for explaining hopping transport.

The activation energy Δ could, in general, be the consequence of an excitation from a localized to an extended state, the result of polaronic effects, or due to trapping by impurities. The latter has been investigated by Gartstein and Conwell in [67], by performing Monte Carlo simulations of the hopping transport of charge carriers. The systems under investigation were determined by both energetic and geometric disorder with the model presented in [65]. Here, however, the bond strengths are randomly assigned the value $w_0 = 1$ with probability p or the value w with probability $1 - p$. Fluctuations in the intersite bond strengths lead to the formation of traps in the form of sites being weakly coupled to all but one of their neighbours, the strong bond being in the direction opposite to the field, so the carriers cannot easily elude such sites. When only geometric disorder is present, a carrier in a trap will leave it via the strong bond for low enough fields, whereas for stronger fields hopping of the carriers through the weak bonds will also become available. In order for the carriers to escape from such traps, an activation energy is therefore required. For a particular degree of disorder, this activation energy is initially enhanced with the field since jumps will occur against the direction of the field, and will reach a maximum when the same number of hops with and against the field

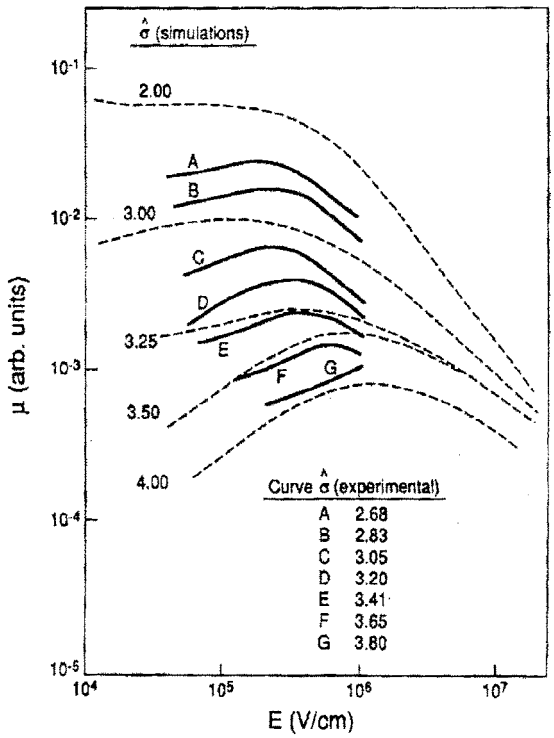

Figure 18. As for figure 17, but with the extra factor $\exp(\Delta/k_BT)$ multiplying μ. Curves A–G are experimental data in which $\hat{\sigma}$ is calculated from the temperature dependence of μ (from [66]).

take place as can be seen in figure 19. However, as the field becomes stronger, weak bonds dominate hopping, and thus the activation energy diminishes. For systems with only energetic disorder present, a trap corresponds to a site of lower energy whose neighbours are sites of higher energy. An increasing field in this case results in reducing the barrier that a trapped carrier has to overcome, leading to reduced activation energy. On the other hand, for systems with both types of disorder, there is the possibility of combined traps, sites of lower energy being connected via weak bonding to sites of higher energies, which cannot be overcome by the field. In this case, the impact of the overall disorder on the activation energy is not simply additive, as can be seen in figure 20, in spite of the opposing behaviour of the two types of disorder. Strong geometric disorder gives a positive slope for the activation energy as a function of the electric field, and strong energetic disorder has the opposite effect. The formation of combined traps will promote an activation energy even for high enough fields, the extent of which depends on the particular details of the representation of disorder.

3.2.1b. Energetic disorder. In contrast to the case of geometric disorder, whose physical justification has been under thorough examination, the choice of a Gaussian distribution for the transporting site energies has been appropriate and well justified. However, it was shown to be an approximation to the density of states, and this motivated the investigation of how hopping transport is affected by the form of the function that describes the density of states [68]. The calculations referred to hopping of charge carriers in a medium both energetically and spatially disordered, at low electric fields, for various temperatures. The medium was constructed by

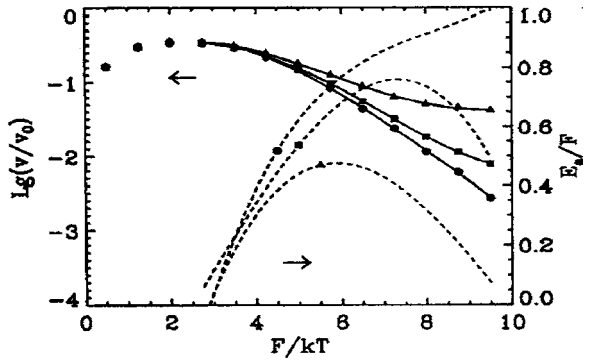

Figure 19. v/v_0 and E_a/F versus $F/(k_BT)$, where v is the drift velocity, v_0 the saturated drift velocity, the activation energy $E_a = -\partial[\ln(v)]/\partial[1/(k_BT)]$, and $F = eaE$ for $w = 0$ (circles), 10^{-5} (squares), and 10^{-4} (triangles) for $p = 0.6$. The solid curves show a least-squares fit to the Monte Carlo simulation data for v/v_0 and the dashed curves give the fits to Monte Carlo simulation data for E_a/F (from [67]).

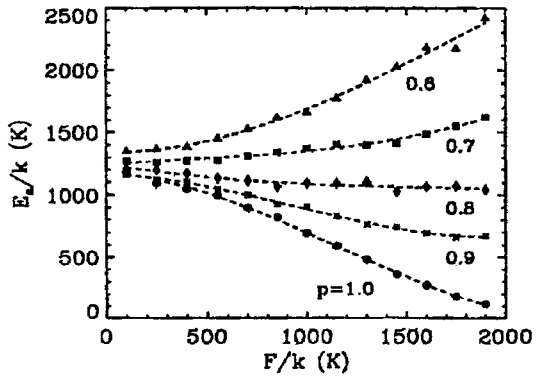

Figure 20. E_a/F versus F/k_B for $p = 0.6$, 0.7, 0.8, 0.9, and 1.0, $w = 0$, and $\sigma = 600k_B$. E_a is determined from an Arrhenius fit to Monte Carlo data at $T = 200$, 250, and 300 K (from [67]).

positioning the transport sites in a completely random fashion, without the support of an underlying lattice.

Three different models were considered for the site energies ε, which were taken as independently distributed random variables. The first model involved the density of states from a distribution uniform over some interval:

$$g(\varepsilon) = \begin{cases} 1/W & 0 \leqslant \varepsilon \leqslant W \\ 0 & W < \varepsilon \end{cases} \tag{33}$$

where W is the measure of the width of the distribution. The second model describes a density of states with a sharp lower and upper cut-off:

$$g(\varepsilon) = p\delta(\varepsilon) + (1-p)\delta(\varepsilon - \Delta). \tag{34}$$

This distribution describes low-energy states ($\varepsilon = 0$) of concentration p and high-energy states ($\varepsilon = \Delta$) with concentration $1 - p$. Finally, a Gaussian distribution was examined, as in the disorder model, but in the absence of a lattice for the transport sites:

$$g(\varepsilon) = (1/\sqrt{2\pi\sigma^2}) \exp\{-\varepsilon^2/(2\sigma^2)\}. \tag{35}$$

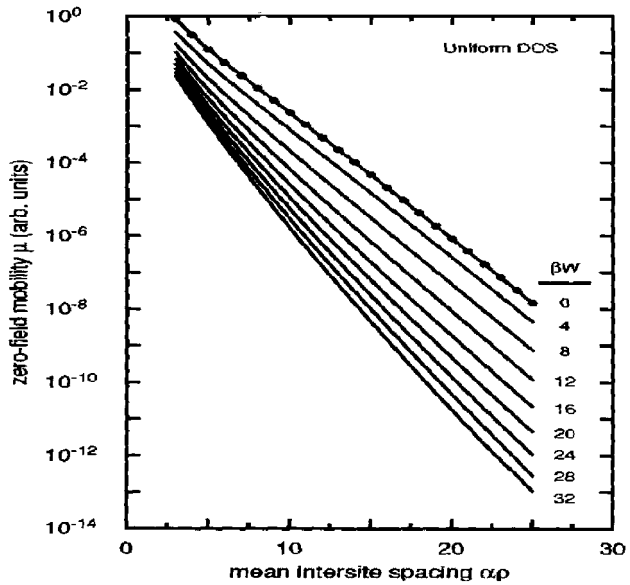

Figure 21. Zero-field μ versus scaled mean intersite distance $\alpha\rho$, where the parameter α gives the effective range of the hopping rate and $\rho = n_0^{-1/3}$, where n_0 is the particle density for a system with a uniform density of states with width W. The top curve corresponds to randomly placed degenerate hopping sites ($W = 0$) and the remaining curves to increasing energetic disorder where W is scaled by $\beta = 1/(k_B T)$ (from [68]).

A uniform density of states, equation (33), is characterized by the crossover between nearest-neighbour hopping for small interparticle distances and variable-range hopping for larger distances. The latter arises from the situation that nearest-neighbour hopping may not occur if they are not of the same energy; figure 21. The binary distribution, equation (34), on the other hand, is associated with the presence of energetic traps. This distribution is important for the low-temperature behaviour of the system, which exhibits a crossover between trap-mediated transport at small intersite distances and trap-limited transport at larger intersite spacings; figure 22. The analysis of the Gaussian distribution, equation (35), has demonstrated an almost exponential decrease of the mobility as a function of the intersite distance, which is typical for hopping; figure 23. A further investigation of the mobility as a function of temperature verified the inverse square temperature dependence $1/T^2$ of the Gaussian model; figure 24. In this case, however, the slope of the $\ln(\mu)$ versus $1/T^2$ curve is a function of the concentration of the transport sites, rather than being constant. This dependence on the concentration has been justified as resulting from the different form of the spatial disorder, in which the absence of a lattice makes it sensitive to the number of transporting sites present.

3.2.1c. The effect of correlations. A problem that characterizes the description of transport in molecularly doped systems with the GDM is its inability to reproduce the Poole–Frenkel behaviour of the mobility, $\ln(\mu) \propto \sqrt{(E)}$, over the entire field range for which it has been experimentally obtained. In order to overcome this deficiency, Gartstein and Conwell [69] suggested that spatially correlated energetic disorder is a necessary requirement for improving the model so as to account for the electric field range of interest. The physical origin of these spatial correlations derives from long-range charge–dipole interactions, which turned out to affect the high-field μ considerably.

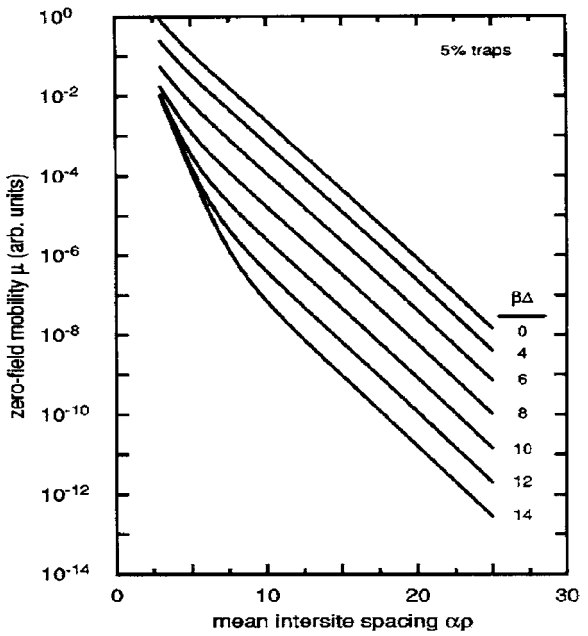

Figure 22. As for figure 21, but for a system with 5% concentration of traps of depth Δ as a function of $a_r = an_0^{-1/3}$ (from [68]).

For the sake of simplicity, the simulation procedure followed involved only diagonal disorder, and the difference from previous calculations of transport was that the site energies ε of neighbouring transporting elements were correlated according to

$$\langle \varepsilon_i \varepsilon_j \rangle = (1/N) \sum_{\alpha n} \sigma_\alpha^2 K_\alpha(r_{in}) K_\alpha(r_{jn}) \tag{36}$$

where N is a normalization factor, and K_α denotes a kernel of neighbouring sites. It turned out that the $\ln(\mu)$ versus $\sqrt{(E)}$ dependence is strongly influenced by the presence of correlations; figures 25 and 26. Both the magnitude of the mobility and its field dependence now change. A sublinear behaviour is observed, which becomes clearer as the disorder is increased. This has been attributed to the fact that in the presence of correlations the random potential wells from which the carrier must escape at each jump have a spatial extent which is the same as the average intersite distance. This smoothing of the random potential renormalizes the energetic effect of the field, which leads to the appearance of the saturation regime at lower fields, and to the extension of sublinear dependence to a bigger range of electric fields than in the uncorrelated GDM.

The importance of spatial correlations in the transport of charge carriers in disordered organic systems was also stressed in later work by Novikov *et al* [70], in which Monte Carlo simulations of three-dimensional systems were performed under the correlated disorder model. As before, the spatial correlations were assumed to come from long-range interactions of the charges with randomly distributed permanent electric dipole moments. The latter produce fluctuations in the potential energy of a charge carrier, which contribute a great deal to the total site energy. In the simulations, two different types of jump rate were examined: the Miller–Abrahams rate for a direct comparison with the Gaussian model, and small-polaron-like rates that reduce exponentially with distance, in order to examine the effect of the form of the hopping rate on the two approaches.

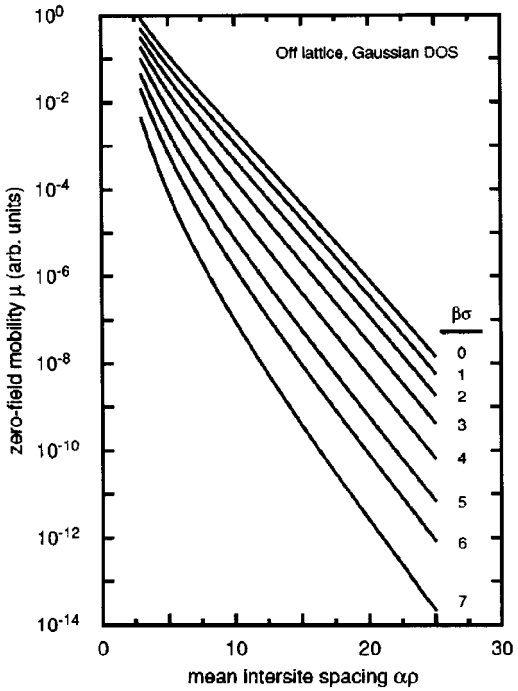

Figure 23. As for figure 21, but for a system with a Gaussian density of states of width σ as a function of $a_r = an_0^{-1/3}$ (from [68]).

The inclusion of the spatial correlations on the transport site energies via the overall interaction of a charge carrier with the dipoles present results in marked extension of the field range for which the Poole–Frenkel dependence of the mobility on the electric field is valid; figure 27. When correlations are included, $\ln(\mu) \propto \sqrt{(E)}$ at low fields as well, whereas in the uncorrelated model the mobility is better described by the form $\ln(\mu) \propto E/(k_B T)$ for the same field interval. The fact that calculations with the initial disorder model were based on the Miller–Abrahams hopping rate leads to a very important restriction of the regime where Poole–Frenkel behaviour is observed, since it causes the mobility to saturate before it follows the $1/E$ dependence at high fields. However, this saturation does not show up when other forms of hopping rate are considered in the initial uncorrelated model; figure 28. This explicit dependence on the form of the jump rate is, on the other hand, absent from the model which includes correlations (figure 29), rendering the Poole–Frenkel behaviour characteristic of transport in molecularly doped polymers, associated mainly with dipole interactions, rather than with electron–phonon interactions which determine the hopping rates.

Apart from demonstrating that spatial correlations due to long-range charge–dipole interactions are necessary for a more appropriate description of transport, in agreement with [69], Novikov *et al* also proposed a different empirical expression for the mobility to equation (3); in particular,

$$\mu = \mu_0 \exp\{-9\hat{\sigma}^2/25 + C_0(\hat{\sigma}^{3/2} - \Gamma)\sqrt{eaE/\sigma}\} \tag{37}$$

where μ_0 may exhibit a temperature dependence due to other less correlated sources of disorder. The choice of this expression was based on a combination of numerical and analytical results, and its applicability was tested in comparison with experimental measurements on

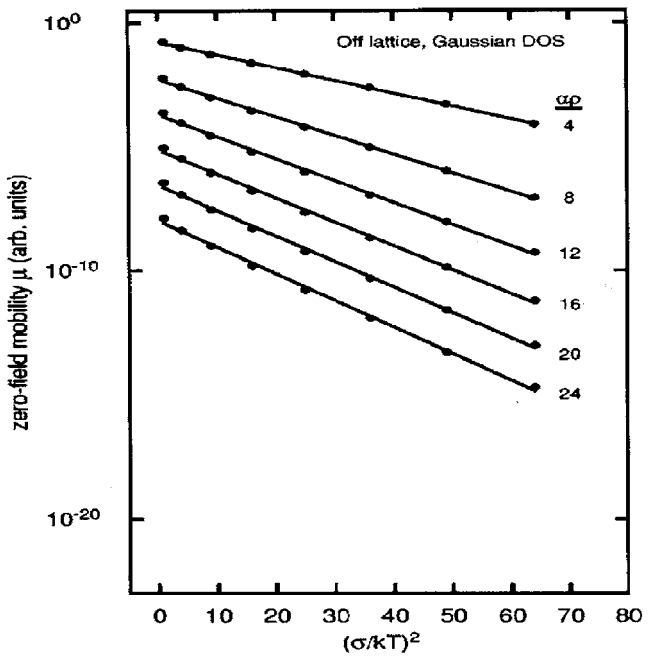

Figure 24. Zero-field mobility μ as a function of the dimensionless parameter $\hat{\sigma}$ for a system of Gaussian density of states of width σ, parametric in the mean interparticle spacing a_r. Transport sites are randomly spaced. Computed data are represented by filled circles; straight lines are numerical fits (from [68]).

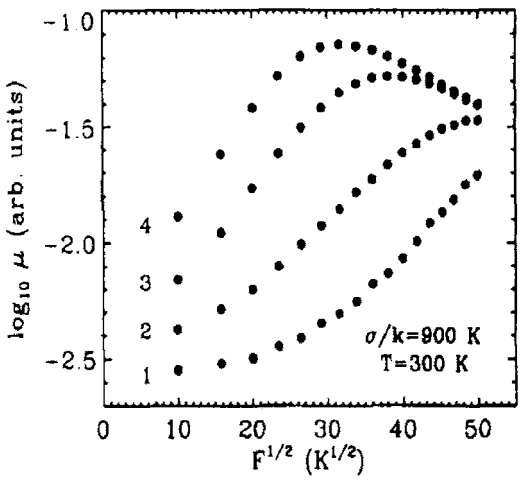

Figure 25. The field dependence of the mobility for systems with an increasing degree of spatial correlations. Here $F = eEa/k_B$ is the potential energy drop due to the applied electric field E between two neighbouring sites of the 'transport' lattice of spacing a in the field direction, measured in units of temperature (from [69]).

organic glasses. The latter examination revealed relatively good agreement with experiment, demonstrating that an alternative view of the mobility dependence of the field and the manner of its determination should be further investigated.

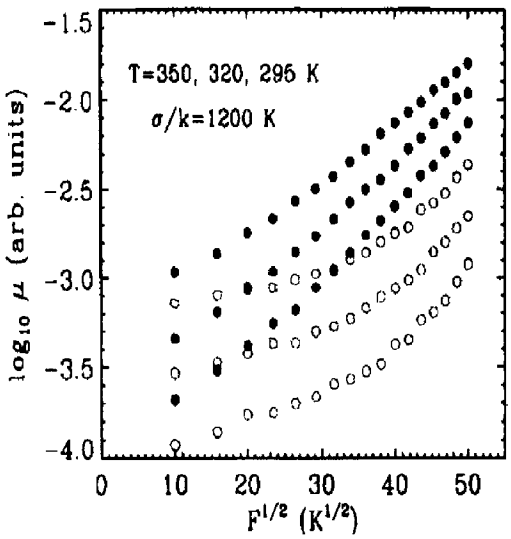

Figure 26. As for figure 25, but for a correlation function f_a (filled symbols) within a sphere of radius a for the temperatures $T = 350, 320, 295$ K from the top to the bottom of the figure, respectively. Open symbols show the corresponding field dependence for a system with the same width of the Gaussian distribution σ but with no spatial correlation (standard disorder model) (from [69]).

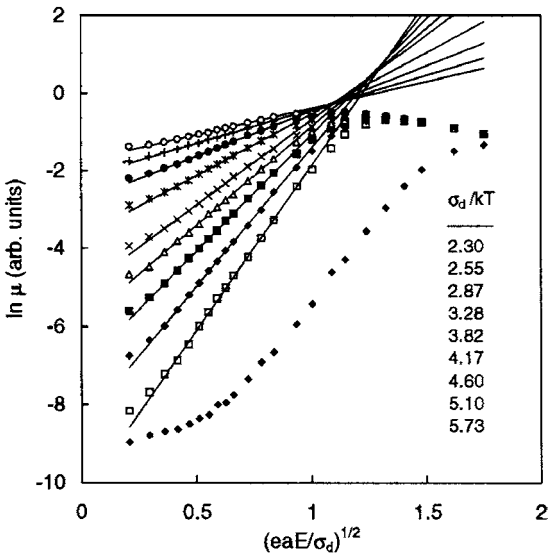

Figure 27. Field-dependent mobility of the correlated disorder model (CDM) for different values of width $\hat{\sigma}_d = \sigma_d/(k_B T)$, where σ_d is the rms width of the dipolar energetic disorder (from the top curve downwards). The lowest curve shows the mobility for the GDM for $\hat{\sigma}_d = 5.1$. If $\sigma_d = 0.1$ eV and the minimum charge–dipole separation is $a = 1$ nm, then $eaE/\sigma_d \approx 1$ for $E = 10^6$ V cm^{-1} (from [70]).

The above discussion demonstrates that failure of the GDM to adequately explain the field dependence of the mobility can be generally attributed to the neglect of spatial correlations

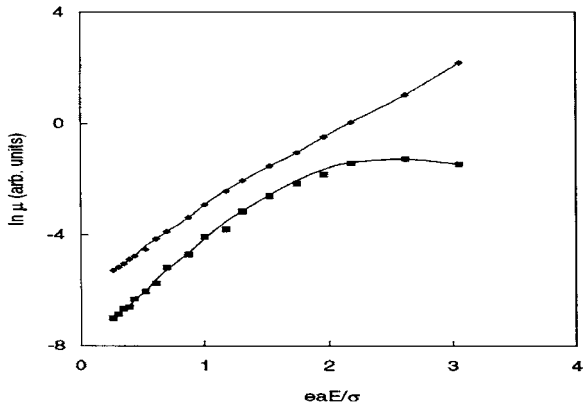

Figure 28. As for figure 27, but for the GDM for $\hat{\sigma}_d = 4.17$ and for two different types of hopping rate: Miller–Abrahams (squares) and symmetric (diamonds) (from [70]).

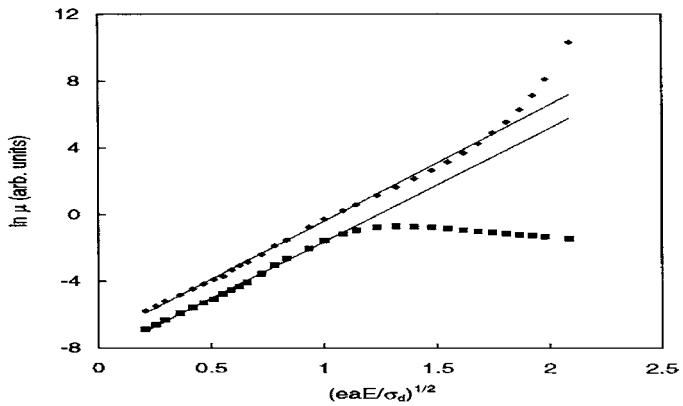

Figure 29. As for figure 28, but for $\hat{\sigma}_d = 5.1$ and two different types of hopping rate: Miller–Abrahams (squares) and symmetric (diamonds) (from [70]).

in the energies of the transporting sites. For the case of molecularly doped systems these spatial correlations were found to be a consequence of the long-range interaction between a transporting charge carrier and the permanent electric dipoles present. This explanation of charge–dipole interactions is not justified, however, for conjugated conducting polymers, in which the concentration of dipoles is negligible. On the other hand, experimental measurements of transport in conjugated polymer films exhibit Poole–Frenkel behaviour for the mobility in an extended field range, which as was discussed before, derives from correlations in site energies. Thus, the transport properties of conjugated polymers should also be affected by spatial correlations.

The origins of such correlations in conjugated conducting polymers were discussed in [71], and two sources were mentioned. First, the variation of the polaron energy with respect to the conjugation length causes fluctuations in the energies of transporting sites, each transporting element being a conjugated polymer segment. Second, as has been demonstrated through measurements of the current–voltage characteristics of such polymers, variations in the film morphology have a significant effect on the energies. In a polymer film there is the possibility of having both crystalline and amorphous regions, the former corresponding to lower energies

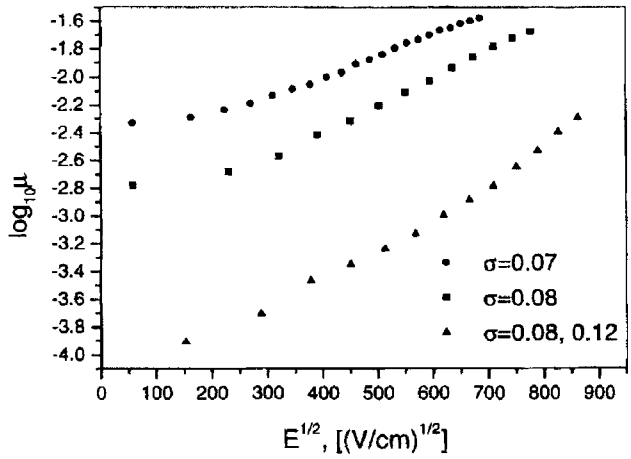

Figure 30. 290 K Monte Carlo results for $\log_{10}(\mu)$ versus $E^{1/2}$ for two homogeneous samples and one inhomogeneous sample with the values of σ indicated and correlation described by equation (38) (from [71]).

due to a larger polarization energy, and the latter characterized by higher energies. Therefore, within a polymer film, regions of analogous degrees of order or disorder should correspond to similar site energies, implicitly leading to short-range site energy correlations.

Monte Carlo simulations were performed for films of conjugated polymers on the grounds of [69] by considering the energy of a specific site to be averaged over the energies of all its k nearest-neighbouring sites; thus

$$\varepsilon = N \sum_{k} \varepsilon_k \tag{38}$$

where N is a normalization factor. Two possible cases were examined: homogeneous systems in which the variance σ of equation (27) was taken to be the same for the entire polymer film, and inhomogeneous systems for which σ had two values. In homogeneous films, stronger disorder leads to smaller values for the mobility since the barriers that a carrier has to overcome become larger; figure 30. Poole–Frenkel behaviour was observed until very high electric fields were reached. For inhomogeneous samples, the same behaviour is observed, with roughly the same slope of the $\ln(\mu) \propto \sqrt{(E)}$ curve, and for the same field range. Despite this qualitative similarity, the calculated mobilities in the second case are almost an order of magnitude smaller. This decrease in mobility could account for the experimental observation that in systems with a high degree of order the mobility is smaller than expected. Although small variance corresponds to a high degree of order, a larger value of σ in part of the sample could be responsible for the reduction in mobility.

It is clear from the aforementioned discussion that in conjugated polymer films the source of correlations is mainly the morphology of the film. In an independent study, the importance of the latter was also stressed, though through a different approach. Yu *et al* [72] have discussed how thermal fluctuations in the molecular geometry introduce spatially correlated fluctuations in the site energies of the electronic excitations. The argument behind this is that the restoring force of these geometry fluctuations, which could be expressed as ring torsions for example, is intermolecular for dense films, resulting in spatial correlations which manifest themselves in the site energies.

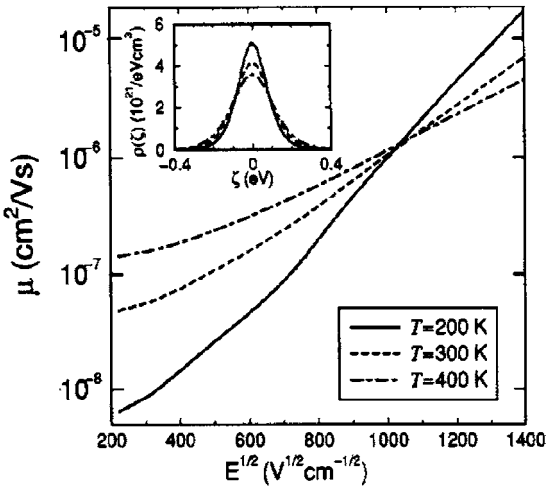

Figure 31. $\log(\mu)$ versus $E^{1/2}$ for different temperatures and for the coupling constant of the polaron and the torsion $\nu = 0.3$ eV, and for intermolecular restoring force constant $K = 0.0034$ eV Å^{-1}. Solid, dashed, and dot–dashed curves correspond to $T = 200$, 300, and 400 K, respectively. The inset shows the distribution of carrier energies at these temperatures (from [72]).

In order to simulate transport in dense polymer films, the Master equation

$$0 = \sum_j \{\omega_{ij} P_j (1 - P_i) - \omega_{ji} P_i (1 - P_j)\} \tag{39}$$

was solved numerically for three-dimensional systems, in which a symmetric hopping rate was used:

$$\omega_{ji} = \omega_0 \exp\{-2\Gamma r_{ij}/a\} \exp\{(\varepsilon(\boldsymbol{r}_i) - \varepsilon(\boldsymbol{r}_j) - e\boldsymbol{E} \cdot \boldsymbol{r}_{ji})/(2k_B T)\} \tag{40}$$

where $\boldsymbol{r}_{ji} = \boldsymbol{r}_j - \boldsymbol{r}_i$.

Calculation of the mobility as a function of the electric field shows the expected Poole–Frenkel behaviour; figure 31. However, the driving mechanism for the mobility depends on the field regime. At low fields the mobility is larger for elevated temperatures, which means that thermal excitations are responsible for overcoming the energy barriers. At high fields, the effect of temperature in mobility is opposite with field-assisted hopping being dominant, so for higher temperatures thermal fluctuations are increased leading to the enhancement of disorder, and thus to a decrease in the mobility.

In the presence of traps (deeper energy levels), the mobility is shown to retain its field dependence, but its magnitude is sensitive to the density of the charge carriers; figure 32. When the carrier density is small, the mobility is also small at low fields, since when a carrier is captured in a trap state, it does not have sufficient energy to escape. An increase in the number of carriers fills the deeper energy levels, quenching these traps and allowing the remaining carriers to become more mobile; thus the mobility becomes larger, especially at small fields.

3.3. Investigations of transport

3.3.1. Effects of spatial disorder. In previous subsections, we examined the GDM which has been the basic approach to the investigation of charge transport in organic disordered media, and we have dealt with various modifications of the model aiming to improve its performance and fit better the experimental findings. The systems of interest are characterized by a great

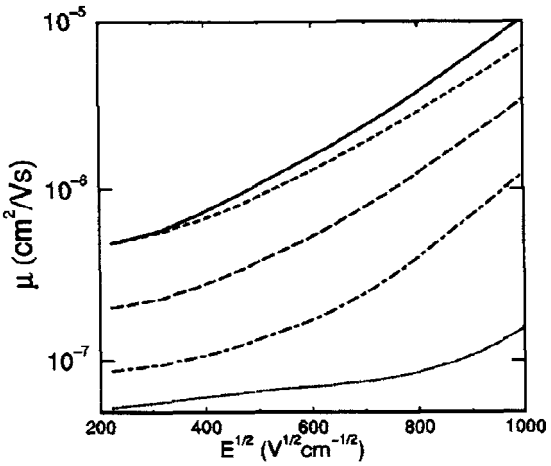

Figure 32. $\log(\mu)$ versus $E^{1/2}$ for different carrier densities for a system with randomly distributed traps. The trap concentration is 0.2×10^{18} cm^{-3} and the trap level is -0.5 eV. Short-dashed, long-dashed, dot–dashed, and dotted curves correspond to carrier densities $n = 0.47, 0.24, 0.12, 0.03 \times 10^{18}$ cm^{-3}, respectively. The solid curve shows the results of solving the linearized Master equation without traps (from [72]).

amount of both energetic and spatial disorder, and we have discussed in detail to what extent spatial effects also determine energetic disorder. As noted in section 1, the technological requirements for control of the mobility (it may not always be desirable to maximize it for balanced transport; see section 2.2.1d) have generated many investigations into how the mobility varies with morphology and composition. It is therefore useful to have hopping models which can calculate the mobility and its field and temperature variation from a model that has an explicit realization of the molecules for small-molecule OEDs and polymers for polymeric OEDs. Other predictions, e.g. $I(t)$ curves, may also be compared with experiment.

In particular, one such study has focused on the effect of spatial disorder and spatial anisotropy of a polymer film on the mobility [73], utilizing the Monte Carlo technique. Spatial disorder was introduced by randomly varying the lattice spacing, whereas anisotropy was incorporated through variations of the lattice constant perpendicular to the direction of the applied field. The systems under investigation were three dimensional and the effect of spatial disorder in all three directions separately was examined; figure 33. When disorder is present only in the field direction, the 3D character of charge transport is emphasized. At low fields, disorder may be overcome by a carrier by choosing a path which comes around a prohibited jump, leading to a slight increase in mobility with the degree of the disorder. However, as the electric field becomes stronger, only jumps along the field direction are accessible, thus reducing the mobility. For further increases in the field, stronger disorder corresponds to lower mobility. When the disorder is applied in the direction perpendicular to that of the field, the mobility decreases with the amount of disorder even in the low-field regime. For the case that spatial disorder is applied in all three directions, the mobility exhibits a combination of the previous two results. For large fields it decreases with respect to disorder, as before, but for low fields the increase in mobility is far more pronounced until the crossover point is reached. Examination of anisotropy shows that a reduction in the lattice spacing transverse to the field direction results in an enhancement of the mobility with disorder, except for very high fields; figure 34. An increase of the lattice spacing, on the other hand, results in a decrease of mobility with disorder for all fields.

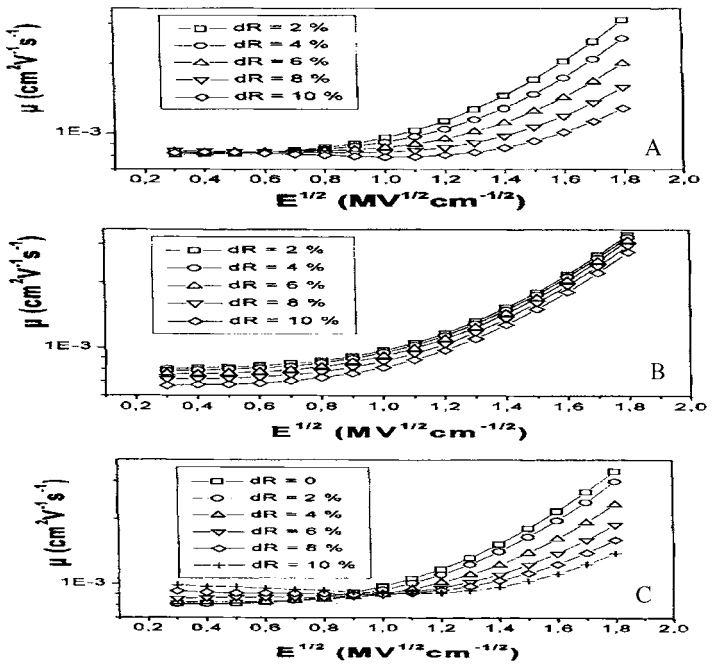

Figure 33. The effect of spatial disorder on mobility ($T = 300$ K, and reorganization energy $E_\lambda = 0.9$ eV). (A) Disorder in the external field direction. (B) Disorder only perpendicular to the external field direction. (C) Disorder in all three spatial directions (from [73]).

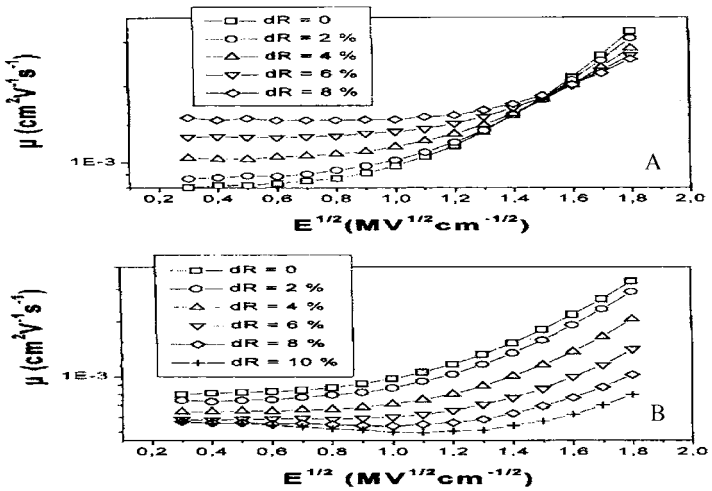

Figure 34. The effect of spatial anisotropy on mobility ($T = 300$ K, $E_\lambda = 0.9$ eV). The external field is in the x-direction. (A) Lattice constant ratios: $x{:}y{:}z = 1{:}0.95{:}0.95$. (B) Lattice constant ratios: $x{:}y{:}z = 1{:}1.05{:}1.0.5$ (from [73]).

In a similar fashion, later work on liquid-crystalline polymer chains has clearly demonstrated that the absence of spatial disorder is a necessary condition for retaining the non-dispersive character of charge transport in polymer films [74]. The Monte Carlo simulation technique was utilized for the description of the motion of charge carriers within a film of

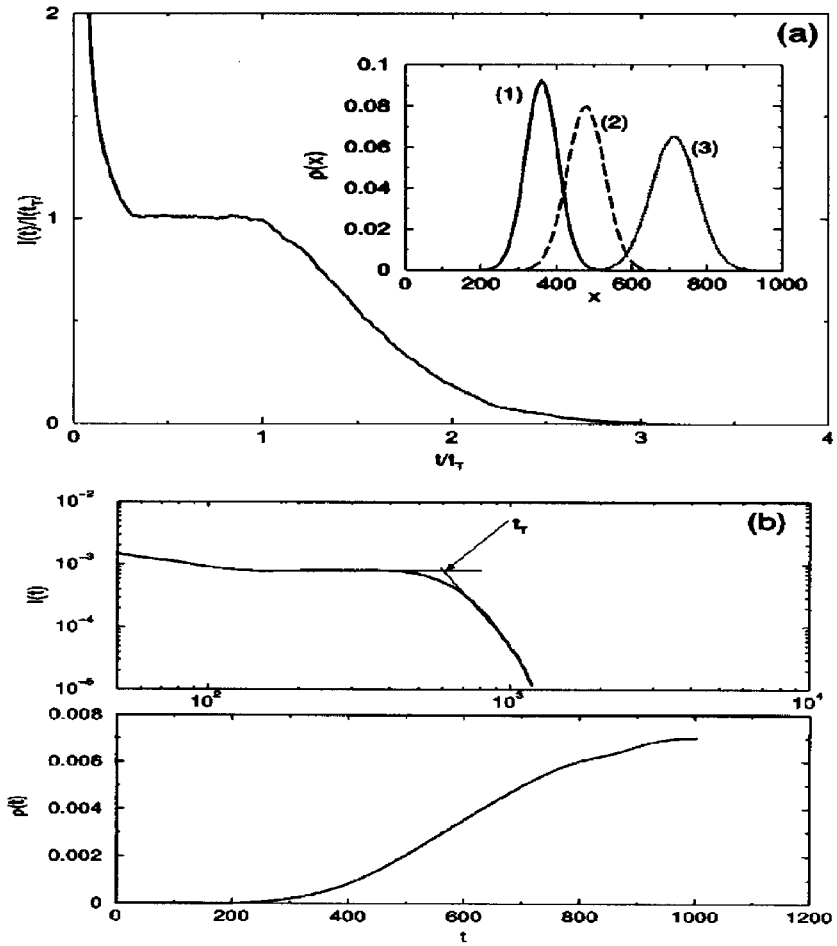

Figure 35. (a) Current versus time for hopping probabilities $p_{+x} = 0.4$, $p_{-x} = 0.1$, $p_{+y} = 0.25$, $p_{-y} = 0.25$. In the inset the charge density is calculated for three different times: (1) $t/t_T = 0.3$, (2) $t/t_T = 0.4$, (3) $t/t_T = 0.6$. (b) The upper plot shows the double-logarithmic representation of the current with respect to time. The arrow indicates the transit time t/t_T. The lower graph shows the charge accumulated at a capacitor connected at the collecting electrode at each time step. In both graphs the axes are in arbitrary units (from [74]).

highly aligned conjugated polymer chains in the form of random walks. The axis of alignment of the film was taken in the direction perpendicular to transport, and despite the need for strong interchain interactions, TOF experiments have shown strong non-dispersive transport, which was clearly reproduced in the simulations (figure 35), by demonstrating the constant plateau in the current transient followed by a long tail, typical of such experiments. However, it was shown that it is possible to change the form of charge transport to dispersive by control of the externally applied field; figure 36. It is generally known that interchain interactions are of the van der Waals form; thus they are relatively weak in comparison with the intrachain interactions. This means that in the system configuration investigated, in which the direction of transport has been chosen to be in the direction of this weak coupling, it is necessary to apply strong fields for adequate transport, which would give enough energy to the carrier to overcome the barrier between different chains. Nevertheless, strong external fields are necessary but not

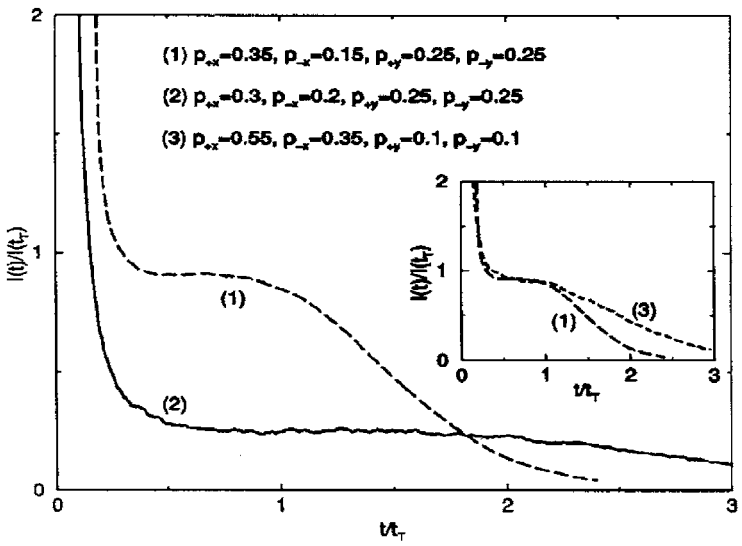

Figure 36. Current versus time for two different strengths of the externally applied electric field E (different hopping probabilities along x). In the inset the current versus time is plotted for two different hopping probabilities along the y-direction (from [74]).

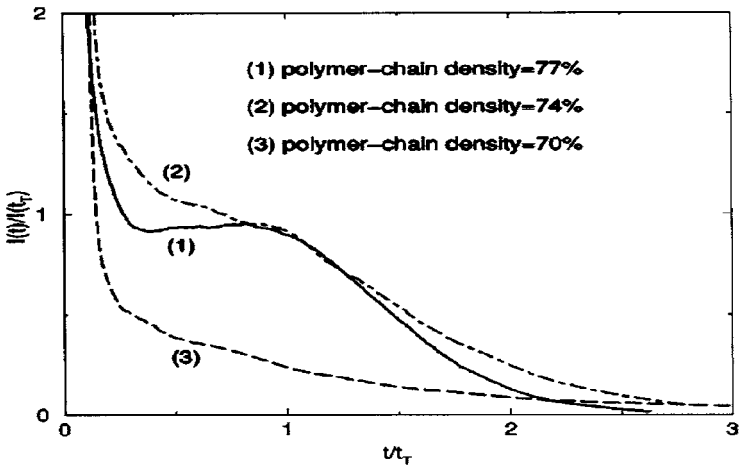

Figure 37. Current versus time for different densities of polymer chains between the two electrodes ($p_{+x} = 0.4$, $p_{-x} = 0.1$, $p_{+y} = 0.25$, $p_{-y} = 0.25$) (from [74]).

sufficient. It turns out that the most important factor for efficient transport is high structural order in the film; figure 37. Even for very strong fields, the presence of traps, which in the case of liquid-crystalline conjugated polymers can be expressed in the form of voids, transforms the character of transport to dispersive. Therefore, one can conclude that charge transport is mainly determined by the degree of positional disorder.

Ramos and Stoneham [75] represented the polymer segments by straight strands of variable length placed on a regular lattice with a variation in orientations. A charge injected into the material follows a simple hopping algorithm. Traps are not included explicitly, but a carrier is described as trapped if

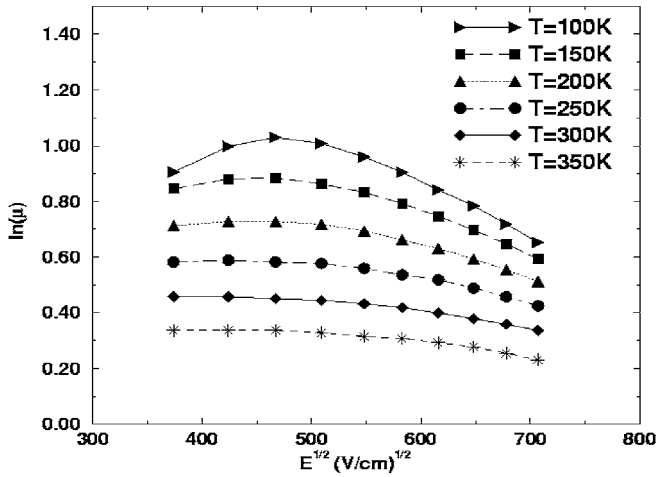

Figure 38. ln(carrier mobility), versus $\sqrt{}$(field), for aligned segments with energetic disorder $\sigma = 0.5k_BT_r$ where $T_r = 300$ K, for temperatures of 100 K (solid curve, sideways triangles), 150 K (dashed curve, squares), 200 K (dotted curve, upright triangles), 250 K (chained curve, circles), 300 K (solid curve, diamonds), 350 K (dashed curve, asterisks) (from [76]).

(a) the total electric field on the charge is zero,
(b) the carrier meets a cross-link and also the electric field is less than a certain critical value, or
(c) the jump probability per time step to a neighbouring chain is $<10^{-5}$.

Quantities such as the luminous efficiency have been predicted. The main conclusions from this work are that the competition between trapping, transport, and recombination leads to systematic trends that can aid in OED design.

The model of Martin *et al* [76] is a random-walk Monte Carlo simulation of hopping transport, in which the polymer film morphology is explicitly included. The polymer chains can be realistically represented as separate segments of random orientations connected to each other for disordered polymers, or they can be of the form of rigid rods for liquid-crystalline conjugated polymers. The model has been recently employed to investigate in detail the effect of both the electric field and the temperature on the mobilities in liquid-crystalline conjugated polymer films. Moreover, various configurations are treated, such as films consisting of perfectly aligned chains all equally spaced, or on irregular positions within the film, and small displacements of the polymer chains from perfect alignment can be included. Also, films made of regions of different alignment are easily constructed.

Such polymer chains are in general very clean systems, and an ideal film would contain chains almost identical to each other. Therefore, the energetic disorder present is small. We have therefore looked at a film of perfectly aligned chains with an energetic disorder that could be attributed to disruptions in the chemical regularity of the chains due to broken bonds or missing atoms. We have assumed the site energies to have a Gaussian distribution with a width σ that is of the order of k_BT_r where $T_r = 300$ K is room temperature. Figure 38 shows the log of the mobility of charge carriers as a function of the square root of the electric field at various temperatures, where $\sigma = 0.5k_BT_r$. The mobility at low temperatures initially increases with field and decreases for larger fields. As the temperature increases the initial decrease disappears and the mobility exhibits a negative slope. The latter is evidence for the saturation of the transit times at higher fields, and is consistent with the discussion in section 3.2. In figure 39, the mobility is shown for an energetic disorder width $\sigma = k_BT_r$. In this case,

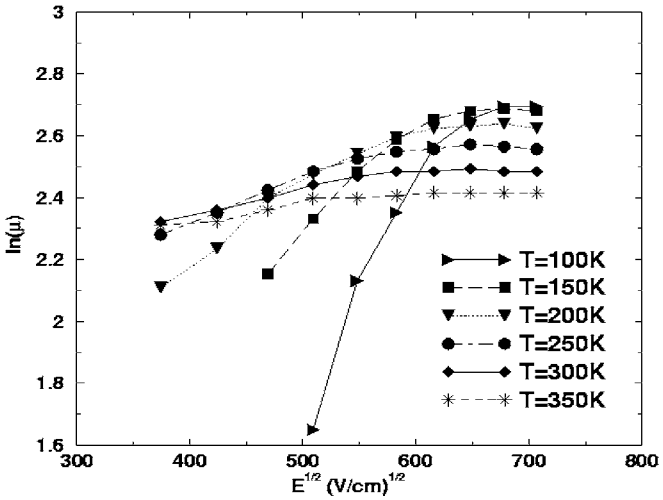

Figure 39. As for figure 38, but for energetic disorder $\sigma = k_B T_r$ (from [76]).

the increase of the mobility with the field and for low temperatures is more pronounced. For low temperatures the thermal energy is not adequate for the charge carrier to overcome any energy barrier that it encounters during its random walk, and, therefore, the mobility increases with the field as the contribution from the electrostatic energy dominates, enabling shorter paths within the film. Nevertheless, as the temperature is increased towards its room value, the effect of disorder diminishes and the mobility exhibits a weak dependence on the electric field with only a slight increase. The mobility behaviour at room temperature is in qualitative agreement with the experimental mobilities of liquid-crystalline polyfluorene films obtained with the TOF technique.

3.3.2. Effects of energetic disorder. Demonstrations of how energetic disorder can influence transport were presented via Monte Carlo simulations of the thermally activated charge transport in one-dimensional disordered systems, under the application of both DC and AC electric fields [77]. In this work the time and frequency dependence of the mobility were studied for the case of two different energetic profiles, one in which the system is described by random energy wells, and the second which is based on random energy barriers. In both cases the jump frequency between two neighbouring sites is given by

$$W_{k\pm} = w_0 \exp\{-E_{k\pm}/(k_B T)\}$$

where w_0 is the attempt frequency. However, for energy wells $E_{k+} = E_{k-}$, whereas for energy barriers $E_{k+} \neq E_{k-}$. In both cases, the random energy values E_k were obtained from a Gaussian distribution.

When the carriers are not in thermal equilibrium at an initial time, the diffusion coefficient, and hence the mobility, might be time dependent. In the case of a DC electric field applied in the direction of the one-dimensional chain, the DC mobilities for the two types of energy profile are identical, decreasing with time; figure 40. Nevertheless, this result should be considered with caution, since it could be the outcome of the one-dimensionality of the system, as the possibility of choosing between different paths in higher dimensions could affect the DC mobility. The application of an AC field, on the other hand, distinguishes between the AC mobility in the well system and that in the barrier system, even for one-dimensional systems; figure 41. In

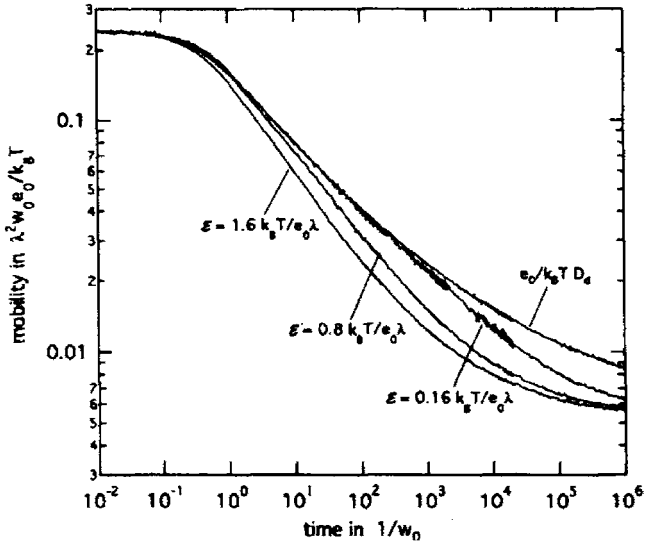

Figure 40. The time dependence of the dc mobility for three different field strengths E (lower curves) and the differential diffusion coefficient D_d for the out-of-the-well (OUW) case. The mobilities are scaled to the zero-field mobility. The scaling factor used is $y/\sinh(y) = 1.001, 1.026, 1.106$, increasing with E (from [77]).

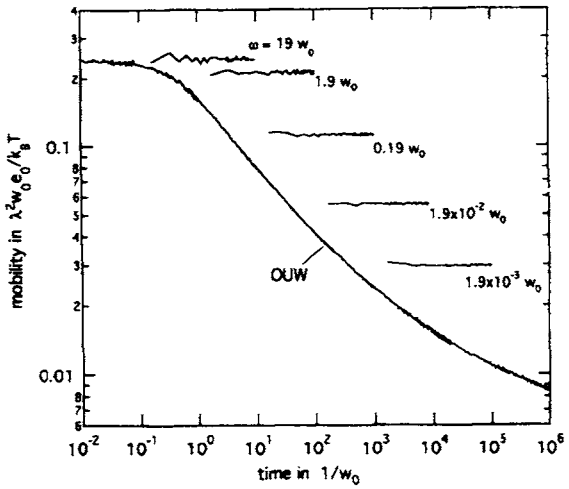

Figure 41. The time dependence of the ac mobility for different frequencies ω. μ_{ac} is independent of ω in the OUW case (decaying trace). In the over-barrier (OVB) case μ_{ac} is constant over time but increases with ω (horizontal traces). $E = 0.16 k_B T/(\varepsilon_0 \lambda)$ for all traces, where λ is the length of the separation between the wells (from [77]).

the former case the mobility decreases with time and does not exhibit any dependence on the frequency of the applied field. In the latter case, the AC mobility does not depend on time, but instead increases with respect to the frequency. It is therefore clear that energetic disorder can have a strong influence on the transport properties of charge carriers in such organic systems.

A more detailed investigation of the mechanisms that govern transport along one-dimensional pathways followed by direct comparison of simulation results with experimental

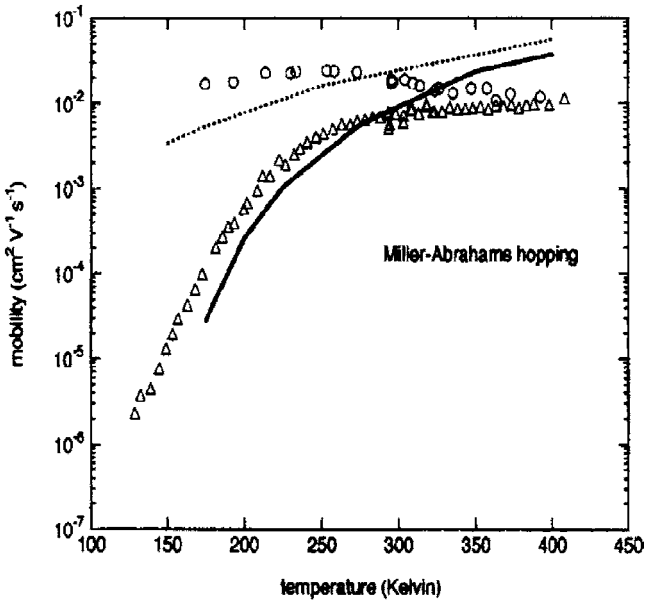

Figure 42. Experimental mobilities of the charge carriers in material T2 versus temperature and the simulated results for the Miller–Abrahams hopping rates. The experimental PR-TRMC and TOF mobilities are shown by circles and triangles, respectively. The dotted and solid curves correspond to the simulation data on ac and TOF mobilities, respectively (from [78]).

data from measurements both under a constant voltage and rapidly oscillating electric fields [78]. The systems of interest were liquid-crystalline discotic materials, in which deviations from perfect stacking result in energetic disorder, as was discussed previously in section 3.2.1c. Charge transport was once again described by the Monte Carlo technique, and emphasis was given to the two aforementioned cases of random energy wells and random energy barriers, as well as the cases of tunnelling-assisted hopping via the Miller–Abrahams model and transport within the framework of polaron formation. The aim of this work was to examine which of the four possible transition rate models describe more adequately the two experimental techniques, each probing different timescales.

The random-energy-well approach was considered to be completely inappropriate for accounting for charge transport through such organic systems, due to the sensitivity of the mobility to temperature. Within this model there exists a critical temperature in which transport changes from Gaussian (non-dispersive) to dispersive, with the mobility becoming independent of time for temperatures above this critical value, but time dependent for lower temperatures. However, this temperature-driven behaviour is in complete disagreement with the experimental high-frequency mobility, which is almost constant for a relatively large range of temperatures. In a similar fashion, the polaronic model can also be discarded as a possible source for explaining charge transport, since it completely failed to reproduce the experimentally obtained results. Neither can the utilization of the Miller–Abrahams model explain the experimental findings, since for TOF experiments the simulated mobility does not agree with the experiments, and for the AC case the mobility appears to be temperature dependent; figure 42. Only the model of thermally activated jumps over random energy barriers from an exponential distribution of energies is capable of describing charge transport for both sets of experimental data; figure 43.

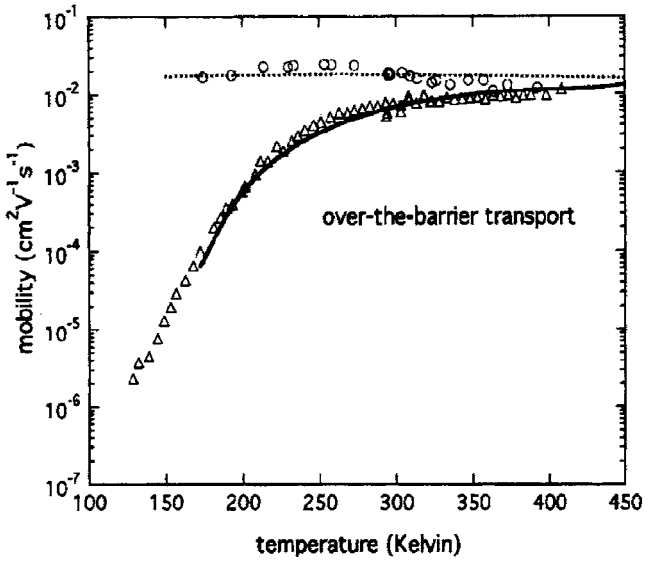

Figure 43. Experimental mobilities of the charge carriers in material T2 versus temperature and the Monte Carlo results for the thermally activated hopping over barriers with an exponential height distribution with width $E_0^b = 0.024$ eV. The experimental data are from the PR-TRMC and TOF measurements are shown by circles and triangles, respectively. The dotted and solid curves correspond to the simulation data on ac and TOF mobilities, respectively (from [78]).

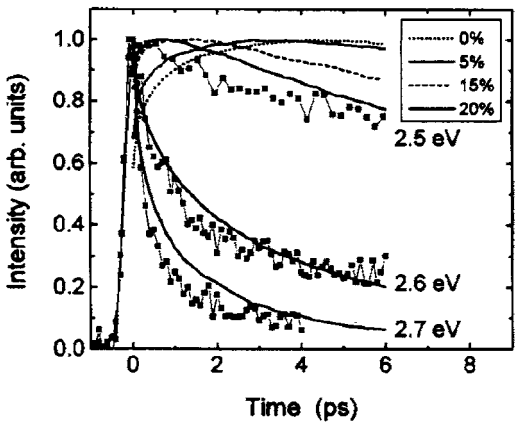

Figure 44. Symbols show the transient luminescence of PPV at different emission energies and at room temperature. The solid curves show the calculation of the transient luminescence for different emission energies and a trap density of 20%. The other curves show the expected luminescence transients at 2.5 eV for lower trap densities (from [79]).

3.4. Numerical simulations of electroluminescence

Apart from the investigation of the transport properties of polymeric materials in electroluminescent devices, the description of other aspects of their operation has also been attempted. In view of this, a Monte Carlo study of the relaxation and dissociation of excitons in conjugated polymers was performed and compared with experiments, which aimed at a better understanding of exciton dynamics [79]. As it turned out, in order to be able to fit the simulation

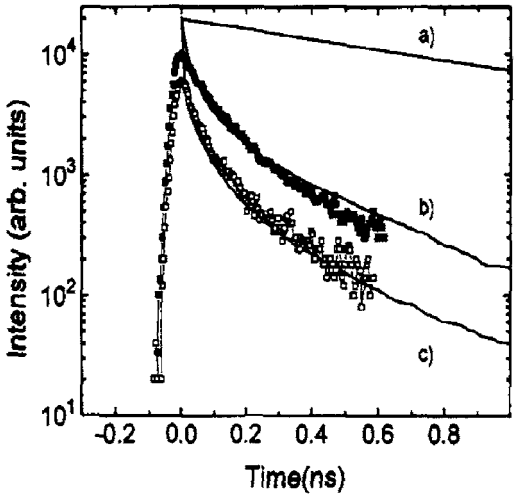

Figure 45. Calculated transient integrated excitation densities for different scenarios: (a) only radiative recombination, (b) radiative recombination and trapping, (c) additional field-assisted dissociation of photoexcitations in an external electric field of 1.5×10^6 V cm^{-1} was considered. The symbols represent the experimental curves without (filled squares) and with (hollow squares) an electric field (from [79]).

results for the time dependence of the intensity with the experimental data, the inclusion of trap states was essential; figure 44. An increase in the concentration of traps corresponds to the appearance of the maximum of the intensity at shorter times. This shift has been attributed to the competition between capture from traps and spectral relaxation towards intrinsic low-energy sites. By increasing the trap concentration in the simulations, it was possible to obtain good agreement with experiments, showing that energetic disorder is also very important for determining the relaxation of neutral optical excitations in conjugated polymers.

In this analysis, the dissociation of excitons into a pair of charge carriers caused by the application of an external field was investigated, since this field-induced dissociation produces a reduction in the photoluminescence. For an exciton to dissociate, the carrier must have enough energy to overcome the Coulomb binding energy of the two charges forming the exciton when located on the same segment and when they have formed a geminate pair, and the external applied field provides this extra energy. It is again necessary to include trapping in the system to fit the experiments, as seen in figure 45. When the system is disorder free, there can be some spontaneous dissociation, but it is only a small effect. With traps, a large number of excitons decay non-radiatively. This luminescence quenching is due to the capture of the electron at the trap site, with the hole remaining on the conjugated polymer chain. Because of the resulting spatial separation of the charged particles in the exciton, the probability for radiative decay is reduced and competing non-radiative processes dominate.

Transient measurements of electroluminescence from organic materials, which involve the application of a voltage pulse and the time response of the signal, exhibit a sudden increase in electroluminescence, which is followed by a further linear increase. After some time the signal then decays exponentially to a steady-state level. A Monte Carlo simulation scheme has been developed [80] to account for the shape of such signals, and to examine the impact of the various parameters which characterize the system. The physical situation under study commences with the bipolar injection of carriers through electrodes with particular barrier heights, under the application of an external electric field. After enough carriers have accumulated on either

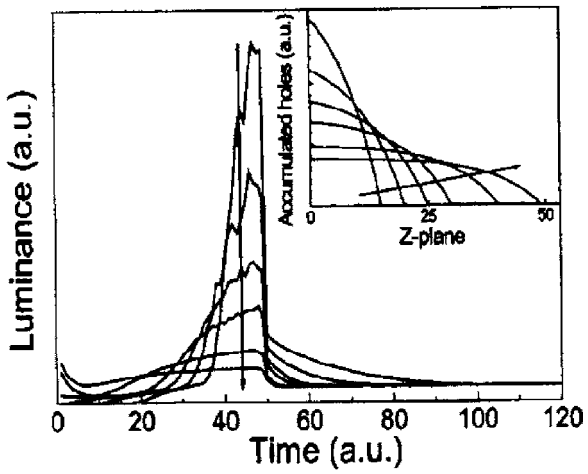

Figure 46. The transient response of the electroluminescence generated by numerical simulation methods for different widths of accumulation regions of electrons and holes in the device. The distribution of the accumulated holes in the device is shown in the inset. The width of the accumulated region W was 15, 20, 25, 30, 40, and 50 lattice units, and the arrows indicate the direction of increase in width (from [80]).

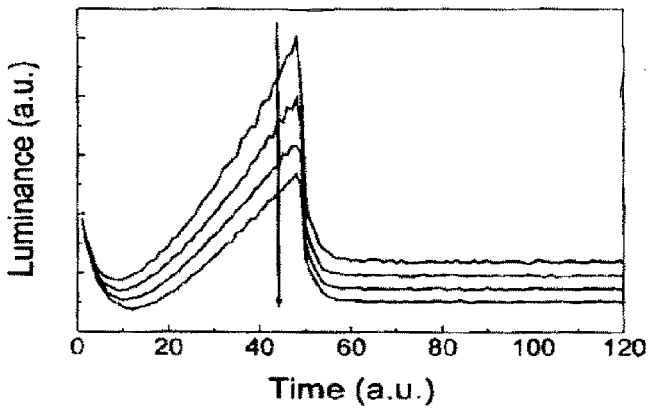

Figure 47. As figure 46, but for different electron barrier heights $\phi_e = 0.4$, 0.6, 0.8, and 1.0 eV, and where the arrow indicates the direction of increase in ϕ_e (from [80]).

contact to ensure equilibrium, they are then allowed to be transported within the polymer film following a Monte Carlo procedure. Recombination takes place when oppositely charged carriers approach each other, and is measured with respect to time.

The initial spike in the electroluminescence signal has been attributed to the extent of the regions near the electrodes where charge is accumulated after injection. To examine the truth of this statement, the width of these regions was initially allowed to vary in the simulations; figure 46. The sharp onset of the signal could only be observed above a threshold for the widths of these accumulation charge layers, which permits adequate overlap between the two carrier densities. On the other hand, variation of the injection barrier heights does not obstruct the sudden peak in the electroluminescent transient (figure 47), leading to the conclusion that only the accumulated charge distribution in the vicinity of the contacts leads to this sharp onset

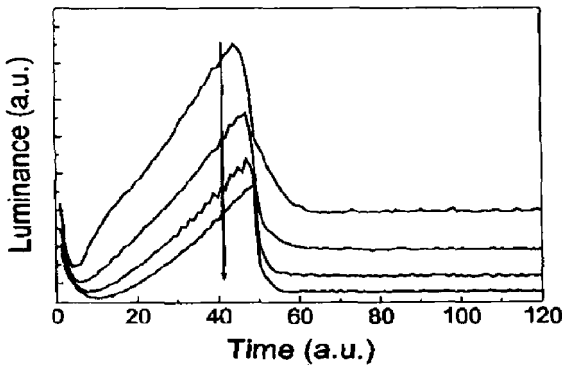

Figure 48. The transient response of the electroluminescence generated by numerical simulation methods where the ratio between hole and electron mobilities has been varied: $\mu_h/\mu_e = 1, 2, 5, 30$, and the arrow indicates the direction of increase in ratio of the mobilities (from [80]).

of the signal. However, the steady-state part of the transient exhibits a dependence on the barrier heights, with decreasing barriers allowing the injection of more carriers, and, thus, the enhancement of the signal. Moreover, the difference between electron and hole mobilities is also seen to have an impact on the signal (figure 48), since the latter decreases as the hole mobilities become larger in comparison to electron mobilities

3.5. Hopping simulations of transport at a contact

Although device contacts have been discussed in terms of continuum device models in section 2, it is clear that treating metal–organic semiconductors analogously to metal–inorganic semiconductor contacts is fundamentally incorrect. In the case of organic semiconductors, carriers are being injected into a disordered solid, with localized states; in the case of inorganic semiconductors, carriers are injected into a continuum of states. In the context of both the continuum band models and the discussion of experimental results, carrier transport is described by either thermionic emission of carriers over a barrier or tunnelling through a barrier. Both of these theories suffer from some limitations. For example, Lupton and Samuel [25] found that upon modelling the injection-limited J–V characteristics of an MEH-PPV device using thermionic emission, the fits to the data broke down at low temperatures. Attempts to fit Fowler–Nordheim tunnelling currents to experimental J–V data only yield a reasonable fit over small portions of the curve, and the height of the barrier to injection determined by a Fowler–Nordheim analysis typically yields a much smaller value than that obtained by direct measurements of the built-in field and the offset between the metal work function and the HOMO level of the material.

In order to produce viable and useful device models which can be used under all conditions, a comprehensive model of injection into organic semiconductors must be developed, which accurately describes the temperature, field, and thickness dependences of J–V characteristics, and should cope with variations in both electrode and semiconductor materials, the latter being both polymeric and molecular. There are several accounts in the literature that attempt to provide a more realistic description of injection from metals into organic semiconductors by explicitly introducing the inherent disorder present in the materials.

Gartstein and Conwell [81] performed a Monte Carlo simulation of emission-limited injection into an energetically disordered molecular insulator, where the transporting sites are represented by a cubic lattice of sites with a Gaussian distribution of energies. The essence of

the model is to calculate the fraction of injected carriers that propagate through the lattice to the opposite electrode. The injection occurs through a simple assumption of injection, suggesting that carriers are thermally excited from the Fermi level into available molecular sites inside the insulator. Transport through the insulator occurs using their previously discussed model. Rather than assuming the photogeneration of carriers in the insulator which is a feature of most Monte Carlo models, this work attempts to move this class of models forwards. The model showed that energetic disorder reduced the yield of carriers crossing the film and more carriers returned to the electrode.

Abkowitz *et al* [82] proposed a model of thermally assisted tunnelling into a trap-free transporting polymer. Their model is based on the premise that thermally assisted tunnelling occurs from states at the Fermi level of the contact into localized transport states of the polymer. The model neglected the effects of energetic disorder, with the transport sites being equienergetic. Transport between different sites in the bulk also occurs by tunnelling. They found good agreement with experimentally obtained J–V data for a PTPB device with a glassy carbon injecting electrode, where neither Fowler–Nordheim tunnelling nor thermionic emission could account for the temperature and field dependence of the J–V characteristics.

Baldo and Forrest [15] developed an interface injection model, in which the presence of interfacial dipoles induces the intermediate states that participate in the injection process. The injection occurs as a two-step process: charges are initially injected into an interface region where the distribution of energy sites is broadened by interface dipoles and lowered due to image charge effects. The limiting step is the hop from the interfacial into the bulk region. Coupling the injection with phonon hopping in the bulk, they obtained good agreement with the thickness and temperature dependence of transport in Al/Alq devices. They also obtained good agreement with J–V characteristics from PPV devices.

Arkhipov *et al* [83] developed an analytic theory for charge injection into OEDs which was found to provide reasonable agreement for the field and temperature dependence of injection-limited current in polymer LEDs. Interestingly, they noted that at high fields, the results obtained resembled Fowler–Nordheim tunnelling even though it was not included in the theory. They then developed a Monte Carlo simulation [84] in which hopping, including hopping from the Fermi level into the dielectric, is performed using the Miller–Abrahams expression. This simulation was found to agree well with the previously obtained analytical expression [85] when considering the field dependence of the yield of charge carriers as a function of the energy barrier at the interface. Finally, they used the Monte Carlo model to investigate the field and temperature dependence of the injection current of an Al/Alq/Mg:Ag OLED, and compared the results to experimental data [86]. They obtained good agreement with the experiment, and noted again the similarity at high fields between the simulated data and Fowler–Nordheim J–V characteristics. They also observed that the injection currents qualitatively resemble those given by Richardson–Schottky thermionic emission over a barrier, although there are quantitative differences between the temperature-dependent behaviour of the simulation and RS emission, and the values of the Richardson constant obtained.

4. Summary and outlook

In this review, we have addressed device modelling for OEDs, both in terms of developing continuum models and more fundamental hopping transport models. Continuum models have been extended to cover charge transport, injection, and recombination, for single-layer and multilayer devices. Time-dependent models and models incorporating coupling to photon states now exist. The latter are essential for devices such as microcavity structures in which optical emission is enhanced, and will prove useful in the design of OED-based lasers. There

has also been a vast amount of effort on developing hopping transport models which aim to explain the field and temperature dependence of the experimentally observed mobilities. Moreover, these models have been successfully applied in the investigation of injection at contacts.

Despite the considerable success of the aforementioned models, there are still outstanding problems to be tackled. For example, continuum device models rely on a large number of material parameters, which are not generally well known. In practice, many parameters such as the density of states can be obtained by looking at similar materials, whilst others, such as carrier mobilities and barriers to injection, can be obtained by fitting to experimental data. More serious perhaps is the inability of the current device models to successfully reproduce device characteristics over a wide range of temperatures or at low fields. The hopping models can be used to predict the mobility, but there are difficulties with regard to variations of both the chemistry and morphology of the materials. At a more fundamental level, whilst they reproduce experimental measurements when correlations are taken into account, the origin of these correlations is not yet known for the whole range of organic materials used, for example in the case of conjugated polymers.

Nevertheless, device models have the potential of being invaluable design tools, as they reduce the number of devices that need to be made by ruling out designs that are unlikely to work. Thus device designers can be selective in their choice of materials and geometries in the devices that are tested. As new materials for use in OEDs continue to appear, modelling is essential for the prediction of their transport properties, which in turn leads to the establishment of fundamental trends in devices employing them. Finally, blends are a topic that has not been addressed here as there has been little attempt to model them, although they are very promising as regards use in both OEDs and photovoltaics.

References

[1] de Leeuw D 1999 *Phys. World* **12** 31
[2] Sirringhaus H, Wilson R J, Friend R H, Inbasekaran M, Wu W, Woo E P, Grell M and Bradley D D C 2000 *Appl. Phys. Lett.* **77** 406
[3] Redecker M, Bradley D D C, Inbasekaran M and Woo E P 1999 *Appl. Phys. Lett.* **74** 1400
[4] Pope M and Swenburg C E 1982 *Electronic Processes in Organic Crystals* (Oxford: Clarendon)
[5] Tang C W and VanSlyke S A 1987 *Appl. Phys. Lett.* **51** 913
[6] Burrows P E, Shen Z, Bulovic V, McCarty D M, Forrest S R, Cronin J A and Thompson M E 1996 *J. Appl. Phys.* **79** 7991
[7] Burroughes J H, Bradley D D C, Brown A R, Marks R N, Mackay K, Friend R H, Burns P L and Holmes A B 1990 *Nature* **347** 539
[8] Phillips P J 1990 *Rep. Prog. Phys.* **53** 549
[9] Campbell I H and Smith D L 2000 *Semiconducting Polymers: Chemistry, Physics and Engineering* ed G Hadziioannou and P F van Hutten (Weinheim: Wiley–VCH)
[10] Wilson J S, Dhoot A S, Seeley A J A B, Khan M S, Kohler A and Friend R H 2001 *Nature* **413** 828
[11] Marshall J M 1983 *Rep. Prog. Phys.* **46** 1235
[12] Mott N F and Davis E A 1979 *Electronic Processes in Non-Crystalline Materials* 2nd edn (Oxford: Clarendon)
[13] Brütting W, Berleb S and Mückel A G 2001 *Org. Electron.* **2** 1
[14] Lampert M A and Mark P 1993 *Current Injection in Solids* (New York: Academic)
[15] Baldo M A and Forrest S R 2001 *Phys. Rev.* B **64** 085201
[16] Crone B K, Davids P S, Campbell I H and Smith D L 2000 *J. Appl. Phys.* **87** 1974 (Fig. 4 © 2000 American Institute of Physics)
[17] Blades C D J and Walker A B 2000 *Synth. Met.* **111–12** 335
[18] Martin S J, Walker A B, Lupton J M and Samuel I D W 2002 *J. Phys.: Condens. Matter* at press
[19] Schmitz C, Pösch P, Thelakkat M and Schmidt H-W 1999 *Phys. Chem. Chem. Phys.* **1** 1777
[20] Cacialli F 2000 *Phil. Trans. R. Soc.* A **358** 173
[21] Friend R H *et al* 1999 *Nature* **397** 121

[22] Bässler H 2000 *Semiconducting Polymers: Chemistry, Physics and Engineering* ed G van Hutten (Weinheim: Wiley–VCH)
[23] Davids P S, Campbell I H and Smith D L 1997 *J. Appl. Phys.* **82** 6319 (Fig. 5 © 1997 American Institute of Physics)
[24] Malliaras G G and Scott J C 1998 *J. Appl. Phys.* **83** 5399
[25] Lupton J M and Samuel I D W 1999 *J. Phys. D: Appl. Phys.* **32** 2973
[26] Kawabe Y, Jabbour G E, Shaheen S E, Kippelen B and Peyghambarian N 1997 *Appl. Phys. Lett.* **71** 1290
[27] Shen J and Yang J 1998 *J. Appl. Phys.* **83** 7706
[28] Tiwari S 1992 *Compound Semiconductor Device Physics* (Boston, MA: Academic)
[29] Barker J A, Foden C L and Greenham N C 2002 *European Conf. on Molecular Electronics* presented paper (available on the Cambridge Display Technology web site www.cdtltd.co.uk)
[30] Sze S M 1981 *Physics of Semiconductor Devices* 2nd edn (New York: Wiley–Interscience) (Fig. 3 © 1981 John Wiley and Sons)
[31] Schroeder D 1994 *Modelling of Interface Carrier Transport for Device Simulation* (Wien: Springer)
[32] Salaneck W R, Stafström S and Brédas J-L 1996 *Conjugated Polymers, Surfaces and Interfaces* (Cambridge: Cambridge University Press)
[33] Fowler R H and Nordheim L 1928 *Proc. R. Soc.* A **119** 173
[34] Campbell A J, Lidzey D G and Bradley D D C 1997 *J. Appl. Phys.* **82** 6326
[35] Pinner D J, Friend R H and Tessler N 1999 *J. Appl. Phys.* **86** 5116 (Fig. 7 © 1999 American Institute of Physics)
[36] Scott J C and Malliaras G G 1999 *Chem. Phys. Lett.* **299** 115
[37] Kawabe Y, Morrell M M, Jabbour G E, Shaheen S E, Kippelen B and Peyghambarian N 1998 *J. Appl. Phys.* **84** 5306
[38] Horio K and Yanai H 1990 *IEEE Trans. Electron Devices* **37** 1093
[39] Ruhstaller B, Carter S A, Barth S, Riel H, Riess W and Scott J C 2001 *J. Appl. Phys.* **89** 4575 (Fig. 8 © 2001 American Institute of Physics)
[40] Lupton J M and Samuel I D W 2000 *Synth. Met.* **111–12** 381
[41] Blom P W M and de Jong M J M 1998 *IEEE J. Sel. Top. Quantum Electron.* **4** 105 (Fig. 6 © 1998 IEEE)
[42] Blom P W M, de Jong M J M and Breedijk S 1997 *Appl. Phys. Lett.* **71** 930
[43] Crone B K, Campbell I H, Davids P S, Smith D L, Neef C J and Ferraris J P 1999 *J. Appl. Phys.* **86** 5767
[44] Tessler N 2000 *Appl. Phys. Lett.* **77** 1897
[45] Scott J C, Karg S and Carter S A 1997 *J. Appl. Phys.* **82** 1454
[46] Martin S J, Verschoor G, Webster M A and Walker A B 2002 *Org. Electron.* accepted
[47] Martin S J and Walker A B 2002 unpublished
[48] Masenelli B, Tutiš E, Bussac M N and Zuppiroli L 2000 *Synth. Met.* **122** 141
[49] Tutiš E, Bussac M N, Masenelli B, Carrard M and Zuppiroli L 2001 *J. Appl. Phys.* **89** 430 (Fig. 10 © 2001 American Institute of Physics)
[50] Davids P S, Saxena A and Smith D L 1995 *J. Appl. Phys.* **78** 4244
[51] Crawford O H 1988 *J. Chem. Phys.* **89** 6017
[52] Chance R R, Prock A and Silbey R 1978 *Advances in Chemical Physics* vol 37, ed I Prigogine and S A Rice (New York: Wiley) p 1
[53] Staudigel J, Stössel M, Steuber F and Simmerer J 1999 *J. Appl. Phys.* **86** 3895
[54] Becker H, Burns S E and Friend R H 1997 *Phys. Rev.* B **56** 1893
[55] Bulović V, Khalfin V B, Gu G, Burrows P E, Garbuzov D Z and Forrest S R 1998 *Phys. Rev.* B **58** 3730
[56] Fisher T A, Lidzey D G, Pate M A, Weaver M S, Whittaker D M, Skolnick M S and Bradley D D C 1995 *Appl. Phys. Lett.* **67** 1355
[57] Tessler N, Harrison N T and Friend R H 1998 *Adv. Mater.* **10** 64
[58] Scott J C, Pautmeier L T and Schein L B 1992 *Phys. Rev.* B **46** 8603
[59] Gill W D 1972 *J. Appl. Phys.* **55** 5033
[60] Frenkel J 1938 *Phys. Rev.* **54** 647
[61] Scott J C, Jones B A and Pautmeier L T 1994 *Mol. Cryst. Liq. Cryst.* **253** 183
[62] Scher H and Montroll E W 1975 *Phys. Rev.* B **12** 2455
[63] Pollak M 1977 *Phil. Mag.* **36** 1157
[64] Bässler H 1993 *Phys. Status Solidi* b **175** 15 (Fig. 11, 12, 13 © 1993 Wiley–VCH)
[65] Gartstein Y N and Conwell E M 1994 *J. Chem. Phys.* **100** 9175 (Fig. 14, 15, 16 © 1994 American Institute of Physics)
[66] Hartenstein B, Bässler H, Heun S, Borsenberger P, Van der Auweraer M and De Schryver F C 1995 *Chem. Phys.* **191** 321 (Fig. 17, 18 © 1995 with permission from Elsevier Science)

[67] Gartstein Y N and Conwell E M 1995 *Phys. Rev.* B **51** 6947 (Fig. 19, 20 © 1995 by the American Physical Society)
[68] Parris P E 1998 *J. Chem. Phys.* **108** 218 (Fig. 21, 22, 23, 24 © 1998 American Institute of Physics)
[69] Gartstein Y N and Conwell E M 1995 *Chem. Phys. Lett.* **245** 351 (Fig. 25, 26 © 1995 with permission from Elsevier Science)
[70] Novikov S V, Dunlap D H, Kenkre V M, Parris P E and Vannikov A V 1998 *Phys. Rev. Lett.* **81** 4472 (Fig. 27, 28, 29 © 1998 by the American Physical Society)
[71] Rakhmanova S V and Conwell E M 2001 *Synth. Met.* **116** 389 (Fig. 30 © 2001 with permission from Elsevier Science)
[72] Yu Z G, Smith D L, Saxena A, Martin R L and Bishop A B 2001 *Phys. Rev.* B **63** 085202 (Fig. 31, 32 © 2001 by the American Physical Society)
[73] Stephan J, Liemant A, Albrecht F and Brehmer L 2000 *Synth. Met.* **109** 327 (Fig. 33, 34 © 2000 with permission from Elsevier Science)
[74] Kambili A and Walker A B 2001 *Phys. Rev.* B **63** 012201 (Fig. 35, 36, 37 © 2001 by the American Physical Society)
[75] Ramos M M D and Stoneham A M 2001 *J. Phys.: Condens. Matter* **13** 2411
[76] Martin S J, Kambili A and Walker A B 2002 unpublished
[77] Hilt O and Siebbeles L D A 1997 *Chem. Phys. Lett.* **269** 257 (Fig. 40, 41 © 1997 with permission from Elsevier Science)
[78] van de Craats A M, Siebbeles L D A, Bleyl I, Haarer D, Berlin Y A, Zharikov A A and Warman J M 1998 *J. Phys. Chem.* B **102** 9625 (Fig. 42, 43 © 1998 by the American Chemical Society)
[79] Scheidler M *et al* 1996 *Phys. Rev.* B **54** 5536 (Fig. 44, 45 © 1996 by the American Physical Society)
[80] Das S, Talapatra G B, Chowdhury A and Pal A J 2000 *J. Appl. Phys.* **88** 6457 (Fig. 46, 47, 48 © 2000 American Institute of Physics)
[81] Gartstein Y N and Conwell E M 1996 *Chem. Phys. Lett.* **255** 93
[82] Abkowitz M A, Mizes H A and Facci J S 1995 *Appl. Phys. Lett.* **66** 1288
[83] Arkhipov V I, Emelianova E V, Tak Y H and Bässler H 1998 *J. Appl. Phys.* **84** 848
[84] Wolf U, Arkhipov V I and Bässler H 1999 *Phys. Rev.* B **59** 7507
[85] Arkhipov V I, Wolf U and Bässler H 1999 *Phys. Rev.* B **59** 7514
[86] Barth S, Wolf U, Bässler H, Muller H, Riel H, Vestweber H, Seidler P F and Riess W 1999 *Phys. Rev.* B **60** 8791
[87] Sze S M 1985 *Semiconductor Devices: Physics and Technology* (New York: Wiley) (Fig. 1 © 2002 John Wiley and Sons)
[88] Tyagi M S 1991 *Introduction To Semiconductor Materials and Devices* (New York: Wiley) p 273 (figure10.8) (Fig. 2 © 1991 John Wiley and Sons)